THESIS FOR THE DEGREE OF DOCTOR OF PHILOSOPHY

Dense gas inflows and outflow-driven shocks in luminous infrared galaxies

Insights from H_2S and other molecules

Mamiko Sato

Department of Space, Earth and Environment
Chalmers University of Technology
Gothenburg, Sweden, 2026

Dense gas inflows and outflow-driven shocks in luminous infrared galaxies
Insights from H_2S and other molecules

Mamiko Sato
ISBN 978-91-8103-304-5

Technical Report No. 5761
ISSN 0346-718X
This thesis has been prepared using LaTeX.

Devision of Astronomy and Plasma Physics
Department of Space, Earth and Environment
Chalmers University of Technology
SE-412 96 Gothenburg
Sweden
Phone: +46 (0)31 772 1000
Email: mamiko@chalmers.se

Cover image: *The Daily Life of a PhD candidate through children's eyes*
Credit: Enrico Shion Sato, Emma Sakurako Sato, and Lovis Kaoruko Sato

Printed by Chalmers Reproservice
Gothenburg, Sweden, Jan, 2026

With reverence for those who defy the sole infinity.

Abstract

Luminous infrared galaxies (LIRGs) are dusty galaxies undergoing a transient evolutionary phase marked by rapid growth through starbursts or active galactic nuclei (AGN). Radiative feedback from these processes is absorbed by dust and re-emitted in the infrared, while mechanical feedback drives outflows that expel gas and dust. Molecular outflows are particularly critical to study, as they directly impact the cold, dense gas reservoir responsible for star formation, sometimes accelerating it to velocities exceeding 1000 km s^{-1}. However, fundamental questions about outflow formation and physical processes remain unresolved.

This thesis investigates hydrogen sulphide (H_2S) as a novel diagnostic for probing dense molecular gas conditions in dusty galaxies and their outflows, with a focus on outflow driving mechanisms. Sulphur-bearing molecules like H_2S are sensitive tracers of shocked, dense gas in AGN and outflows, offering unique insights into chemical and physical environments. Observations with the Atacama Pathfinder Experiment (APEX) and IRAM Northern Extended Millimetre Array (NOEMA) (Paper I) reveal new H_2S detections in LIRGs. At the resolution of these data, H_2S abundance enhancements are not directly linked to outflows, but we identify a potential connection between dense gas reservoirs and feedback properties. The similar infrared–H_2S and infrared–H_2O correlations suggest shared emission origins, likely from warm gas in shocks or regions irradiated by star formation or AGN.

In Paper II, we expand this analysis with ALMA Band 5 observations of the ortho-H_2S $1_{1,0}$–$1_{0,1}$ transition in NGC 1377, NGC 4418, and NGC 1266. Compact H_2S emission (<150 pc scales) is detected in all three galaxies, with broad line wings indicative of outflowing or shocked gas. NGC 4418 exhibits counterrotating H_2S kinematics and a peculiar redshifted feature, possibly tracing inflowing gas or a slanted outflow. Radiative transfer modelling (RADEX) constrains the H_2S-emitting gas to extreme densities ($n_{H_2} \gtrsim 10^7$ cm^{-3}) and warm temperatures (40–200 K), surpassing densities inferred from CO. This confirms H_2S as a selective tracer of ultra-dense molecular gas, likely influenced by AGN or starburst-driven shocks.

In Paper III, we focus on one galaxy NGC 4418, a dusty LIRG hosting a compact obscured nucleus (CON). To investigate further the possible counter-rotation, we analysed the ALMA data with higher spatial resolution (0".05). The possible interpretations of the observation results are discussed through kinematic modelling for H_2S emission line and comparison with other species.

In summary, this thesis demonstrates that H_2S is frequently enhanced in shock- and feedback-dominated regions associated with star formation or AGN activity within the heavily obscured environments of galaxies, highlighting a connection between nuclear dense gas reservoirs and molecular outflows in their central regions. It also presents evidence of complex nuclear gas dynamics, including inflow, outflow, and possible counter-rotation, in one of the studied galaxies. This work touches upon the possible origin of H_2S enhancement, the fate of the dense outflowing gas and the long-term implications for galaxy evolution, while the detail aspects will remain a matter of investigation in future studies. Altogether, these results provide new insights into the life cycle of gas in the inner regions of infrared-luminous galaxies and emphasise the importance of multi-species, high-resolution observations for investigating feedback and the chemical evolution of galaxies.

Keywords: Galaxies:ISM - ISM: molecules - ISM: outflows.

List of Publications

This thesis is based on the following publications:

[A] **M. T.Sato**, S. Aalto, K. Kohno, S. König, N. Harada, S. Viti, T. Izumi, Y. Nishimura, and M. Gorski, "APEX and NOEMA observations of H_2S in nearby luminous galaxies and the ULIRG Mrk 231". Astronomy & Astrophysics, Volume 660, A82, 2022.

[B] **M. T.Sato**, S. Aalto, S. König, K. Kohno, S. Viti, M. Gorski, F. Combes, S. García-Burillo, N. Harada, P. van der Werf, J. Oter, S. Muller, Y. Nishimura, J. S. Gallagher, A. S. Evans, K. M. Dasyra, and J. K. Kotilainen, "High-resolution ALMA observations of H_2S in LIRGs: Dense gas and shocks in outflows and CNDs". Astronomy & Astrophysics, Volume 702, A156, 2025.

[C] **M. T.Sato**, S. Aalto, S. König, "Complex Nuclear Gas Flows in NGC 4418: H_2S as a Tracer of Infall and Outflow
With Supporting Multi-Line Evidence from HNC, CH_3OH, and H_2O". In preparation, 2026.

Other publications by the author, not included in this thesis, are:

[D] N. Falstad et al., **M. Sato**, "CON-quest Searching for the most obscured galaxy nuclei". *Astronomy & Astrophysics 649, A105*, 2021.

Acknowledgments

First, I would like to thank my supervisor Susanne Aalto for her support, patient guidance and encouragement along this path until here, but most of all and to begin with, for giving the enlightenment to this opportunity, that it actually is possible to study again after having a family. Many thanks are owed to my examiner, Wouter Vlemmings, for helpful and realistic suggestions. Sabine König is the person whose limit of patience has been tested most by my slow learning. My admiration and respect are hers, thank you so much. I also appreciate Per Bjerkeli and Mark Gorski for their constructive and pedagogical explanations answering my spontaneous questions. Special thanks also go to my another supervisor, Kotaro Kohno, for continuing his support throughout several phases of my academic life. Daniel Tafoya has devoted his time to answering any questions I had related to research, always responding whenever I asked. Through his passion for science, I learned the philosophy on which a scientist should stand. I am truly grateful for his support during my proto-academic life and feel fortunate to have encountered one of the rarest kinds: a genuine scientist.

I would like to specially thank Kirsten Knudsen for her warm-hearted solicitude. I have survived several transitions in my life over these years largely thanks to her. She is undoubtedly a role model for me. The greatest fortune of my rather long PhD life has been the privilege of having many great colleagues. Many thanks to Madeleine Y., Ramlal, Behzad, Miora, Kiana, Gustav, Siddharth, Santiago, and Clare in addition to all I mentioned in my Licentiate thesis, and many others for being there and directly and indirectly encouraging me to keep going.

Finally, tack så himla mycket, mina kära söta tre apor! You guys have developed into such upright individuals, despite all the constraints I had to impose on you. I am truly the luckiest person to have had the opportunity to grow up alongside such pure-hearted, healthy children.

Contents

CHAPTER 1

Introduction

Galaxies are the fundamental building blocks of the Universe. They are composed of stars and an interstellar medium of gas and dust. Many galaxies undergo evolutionary phases of rapid, dust-enshrouded growth, characterised by intense star formation (starbursts) and black hole accretion in their centres. The resulting nuclear activity produces feedback in the form of radiation, which is absorbed and re-emitted by dust, and through powerful outflows. This mechanical feedback can expel gas from galaxy centres, and in some cases the ejected material may even reach intergalactic space. Understanding the physical conditions, mass, velocity, and morphology of these outflows is essential for determining their role within the broader framework of galaxy evolution (Arroyave, Cicone, et al. 2024; Fluetsch et al. 2021).

The molecular clouds serve as the primary reservoir from which new stars form, and their distribution and physical state regulate both the instantaneous and long-term star formation rates of galaxies. In systems with high gas column densities, particularly luminous and ultraluminous infrared galaxies (LIRGs and ULIRGs), extreme starburst activity is triggered by interactions or mergers that funnel large amounts of gas into the inner few hundred parsecs. These environments are often heavily obscured at optical wavelengths due to dust-enshrouded star formation and deeply embedded active galactic nuclei (AGN). Consequently, the molecular gas component becomes crucial for understanding their energetics and evolution (Israel et al. 2023).

Star formation and AGN activity generate significant feedback on the surrounding medium through radiation pressure, stellar winds, supernova explosions, and AGN-driven outflows. These processes drive large-scale motions of molecular gas, including inflows that feed central activity and outflows that regulate star formation and redistribute material. In the nuclei of LIRGs, where obscuration is extreme, optical and near-infrared tracers are often

difficult to observe, and the kinematics of the dense molecular gas must be probed through millimetre and submillimetre emission lines. While species such as CO, HCN, and HCO^+ are commonly used, they may become optically thick or insensitive to certain physical conditions (Aalto et al. 2011; Fluetsch et al. 2021; Israel et al. 2023). This motivates the search for additional molecules capable of tracing deeply embedded gas motions.

In this context, the rotational transitions of hydrogen sulfide (H_2S) offer a promising diagnostic for identifying and characterising nuclear activity in highly obscured environments. H_2S emission arises primarily from warm, shocked, dense gas and is less sensitive to optical depth limitations than many conventional tracers enabling the detection of compact, energetically driven structures within (U)LIRGs. This thesis investigates the utility of H_2S as a kinematic proxy for feedback processes by analysing a sample of galaxies and presenting high-angular-resolution ALMA observations of one system in particular. The goal is to assess how H_2S emission traces molecular gas dynamics and to evaluate its effectiveness in revealing the internal structure and evolution of dusty, infrared-luminous galaxies.

1.1 (Ultra) Luminous Infrared Galaxies ((U)LIRGs)

General references: Sanders & Mirabel (1996), Pérez-Torres et al. (2021)

1.1.1 Discovery and classification of (U)LIRGs

The first all-sky survey at far-infrared wavelengths was carried out in 1983 by the Infrared Astronomical Satellite (IRAS) and resulted in the detection of tens of thousands of galaxies, the majority of which were too faint to have been included in previous optical catalogues. Here started the identification of a class of "infrared galaxies", objects that emit more energy in the infrared ($\sim$ 5-500 μm) than at all other wavelengths combined. Among them, (U)LIRGs are defined by having excessive infrared luminosities ($L_{\rm IR} > 10^{11} L_\odot$ and $> 10^{12} L_\odot$, respectively). Recent studies show that most (U)LIRGs are part of close interactions or are mergers of molecular gas-rich spirals. When galaxies interact with each other, large masses of gas and dust are funnelled to their central regions. This leads to a dense, dusty and molecular-rich region in the centre of the galaxy. The dust absorbs ultraviolet (UV) emission from young stars or from the accretion onto a supermassive black hole (SMBH) - a so called Active Galactic Nucleus (AGN). This emission is then re-radiated as infrared emission. There is an ongoing debate if star formation, or an AGN, dominates the thermal infrared emission.

Gao & Solomon (2004b) presented a tight correlation between the infrared luminosity ($L_{\rm IR}$) and the luminosity of the hydrogen cyanide 1-0 line emission, $L_{\rm HCN}$, as evidence of star formation being the main power source of the (U)LIRGs. This can be argued, assuming that $L_{\rm IR}$ is a measure of the star formation rate (SFR), and $L_{\rm HCN}$ indicates the mass of the dense molecular gas. Gao & Solomon (2004b) find that this correlation is valid in normal spiral galaxies, LIRGs, and ULIRGs alike (Fig. 1.1).

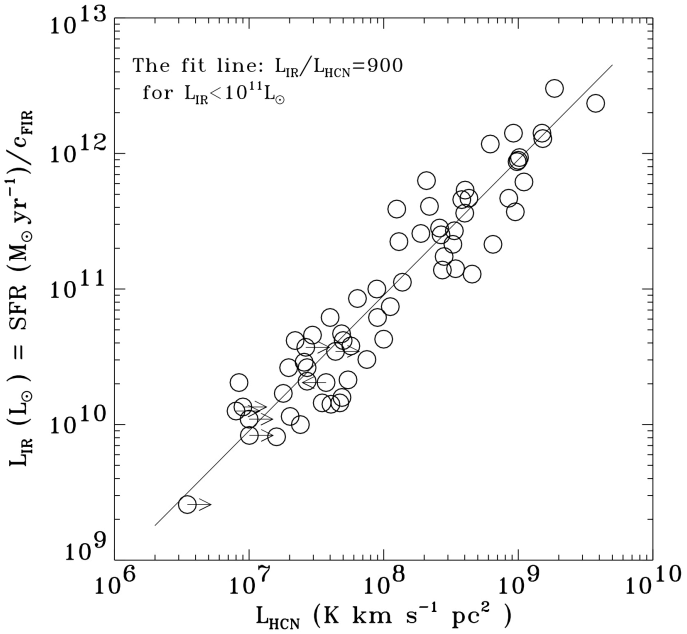

Figure 1.1: Correlation between HCN and IR luminosities in 65 galaxies (Gao & Solomon 2004b)

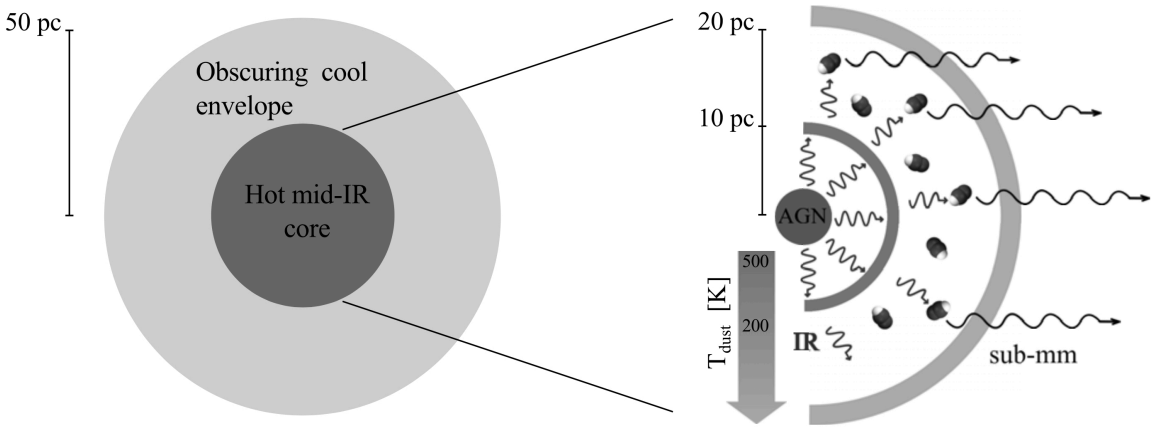

Figure 1.2: Schematic drawing of CON (credit: F.Costagliola). It shows how HCN molecules absorb buried mid-infrared emission and then re-radiates this emission at longer wavelengths.

1.1.2 Compact Obscured Nuclei (CONs)

Since (U)LIRGs are in general highly dust-enshrouded objects, the dust hides very active evolutionary phases of nuclear growth. Some (U)LIRGs host extremely compact (r <100 pc) and dust obscured nuclei with visible extinction $A_V \gg$1000, corresponding to a column density of the H_2, $N_{H_2} > 10^{24}\mathrm{cm}^{-2}$. These regions are categorised as Compact Obscured Nuclei (CONs), in Aalto et al. (2015b). At these high levels of extinction, the large amount of obscuring material hampers optical, mid- and near-infrared and X-ray observations and one has to use far-infrared and/or sub-mm/mm lines and continuum to probe the activity within these most enshrouded galaxy nuclei.

For regions where column densities are above 10^{24}, but below $10^{25}\mathrm{cm}^{-2}$, radiatively excited molecular emission lines of e.g., H_2O and OH are good probes of the nuclei in the far-infrared ($\lambda \approx$ 30-660 μm). At longer radio wavelengths (λ in cm) OH mega-masers are commonly seen in ULIRGs, and also H_2O masers are found associated with AGN accretion discs or in post-shock gas along nuclear jets (see a review by Lo (2005)). Several CONs have N_{H_2} in excess of $10^{25}\mathrm{cm}^{-2}$ and in some cases column densities may reach extreme values of $> 10^{26}\mathrm{cm}^{-2}$. The nearby LIRG-CON, NGC 4418, is likely one example and an N_{H_2} in excess of $10^{26}\mathrm{cm}^{-2}$ has been suggested for the LIRG IC 860 and for the ULIRG Arp 220 (e.g., Aalto et al. 2019; Scoville et al. 2017).

The intense infrared radiation arising from warm dust (100-300 K) in these sources dominate a significant fraction of the bolometric luminosity of the galaxy and effectively excite vibrational levels of molecules such as HCN. Sakamoto et al. (2010) reported the first detection of strong line emission from the rotational transitions of the vibrationally excited v_2=1 state of HCN (HCN-vib) in external galaxies at (sub-)millimetre wavelengths (HCN 3-2 v_2=1:267.2GHz, HCN 4-3 v_2=1: 356.3GHz). HCN-vib requires a mid-IR surface brightness of over 5 $\times 10^{13} L_\odot/\mathrm{pc}^2$ to be excited (Aalto et al. 2015b). For an illustration of HCN absorbing buried mid-infrared emission and re-emitting it at longer wavelengths, see Fig. 1.2. The large H_2 column density in the CON regions will also result in luminous dust emission in the mm- and submm-range. Falstad et al. (2021) discussed on the link between HCN-vib and the mm-continuum surface brightness in detail. The emitting region should be either an extremely compact opaque starburst, or an obscured AGN.

Falstad et al. (2021) defined CONs as galaxies with strong HCN-vib $l = 1f, J = 3-2$ transition line emission ($\Sigma_{\mathrm{HCN-vib}} > 1 L_\odot \mathrm{pc}^{-2}$) from a region with radius $r > 5$ pc. A CON is also defined as having a lower limit of $L_{\mathrm{HCN-vib}}/L_{\mathrm{IR}} > 10^{-8}$. Falstad et al. (2021) found CONs in almost 40% of a volume limited sample of ULIRGs in an ALMA survey, and in 20 % of the LIRGs. No CONs were found in a local sample of sub-LIRGs with L_{IR} of $10^{10} L_\odot$. Their ALMA survey (named CONquest) was limited to a total of 38 galaxies and a larger survey is important for a full census of CONs. There have been several observations searching for CONs, but so far, luminous HCN-vib line emission has primarily been found in ULIRGs and in LIRGs that appear to be early type spirals (e.g., Aalto et al. 2015a,b, 2016, 2019; Falstad et al. 2021; Imanishi & Nakanishi 2013; Imanishi, Nakanishi, & Izumi 2016; Martín et al. 2016).

1.1.3 Inflows and outflows in CONs

The central regions of CONs show evidence of reversed P-Cygni profiles in molecular and atomic lines, indicating inflowing gas (e.g., Aalto et al. 2015a, 2019; Costagliola et al. 2013; Falstad et al. 2021; González-Alfonso et al. 2012; Sakamoto et al. 2013). Therefore, there has been a suggestion that CONs may represent a short phase in the galaxy's evolution which is occurring before the feedback from the starburst/AGN becomes important, before an outflow develops enough to be detected (see Falstad et al. 2019, for a discussion). However, recent mm- and cm-wave studies of some LIRG- and ULIRG-CONs reveal fast outflows, for example, the collimated outflow in Arp 220 (Barcos-Muñoz et al. 2018). More studies of the morphology and extent of outflows are necessary to understand what role the outflows play in CONs.

1.2 Feedback: outflows

General references: Veilleux et al. (2020), Veilleux, Cecil, & Bland-Hawthorn (2005)

1.2.1 Overview of galactic outflows

Galaxy centres can be fed with gas and dust during mergers or more distant interactions with other galaxies. On the other hand, they also expel part of the material of which they are constituted, like gas and dust, in large-scale galactic outflows. Such mechanisms of accretion and feedback of mass, momentum and energy regulate the physical processes which occur within galaxies, which in turn determine important parameters such as star formation rate, chemical composition, and stellar populations. For example, star formation could be quenched due to the mass-loss occurring as a result of an outflow. Mass-loss from a galaxy nucleus also has an impact on the black-hole growth. Consequently, by studying the processes of inflowing and outgoing gas and dust, including the mass and physical conditions of the out- and inflows, it is possible to understand the evolutionary state of a galaxy.

The role of outflows as a mechanism of feedback is of particular importance because they can transfer and distribute mass, energy and momentum from small to large scales. Outflowing gas is commonly seen from a variety of galaxies, which include (U)LIRGs hosting a starburst and/or an AGN.

Outflows can occur on different size scales in a galaxy. There is also observational evidence of large-scale narrow-angle/jet-like outflows from several Seyfert galaxies, which might be mainly AGN-driven, as suggested from their morphology and orientation.

Outflows have been identified at different wavelengths: optical, infrared, radio, UV and X-rays, suggesting that outflows are multi-phase with both hot and cool gas components. For example Mrk 231, a nearby ULIRG and quasar, has a neutral gas outflow observed in the molecular and atomic phases on scales of a few hundreds of parsecs (e.g. Cicone et al. 2012; Morganti et al. 2016). NGC 1365, a barred spiral Seyfert galaxy, has an outflow of ionised gas on scales extending over a few kilopersecs (Venturi et al. 2017, 2018). Gao et al. (2021) reported a high-resolution CO 1–0 map of NGC 1365, showing noncircular motion of molecular gas, reaching a velocity of up to 100km s^{-1}, which is comparable to that of the ionised gas.

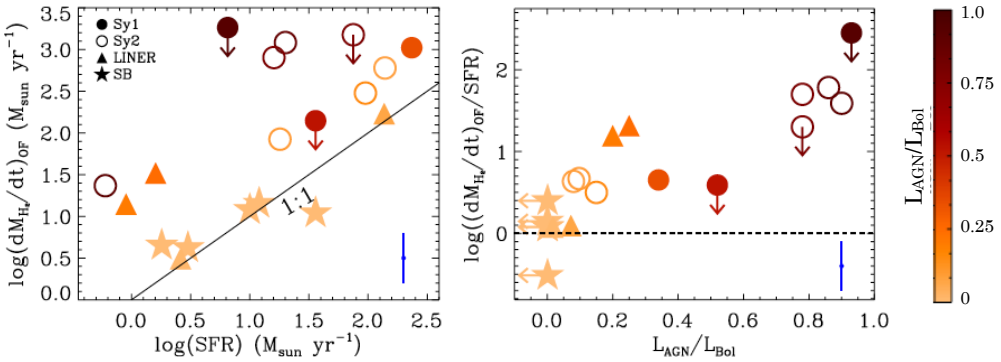

Figure 1.3: *left*: outflow mass-loss rate as a function of the star formation rate for the extended sample of galaxies. Filled and open circles represent unobscured and obscured AGNs, respectively. LINERs are plotted as upward triangles and "pure" starburst galaxies as stars. Symbols are colour-coded according to the fraction of bolometric luminosity attributed to the AGN ($L_{\rm AGN}/L_{\rm Bol}$).The black dashed line represents the 1:1 correlation between SFR and outflow mass-loss rate. *right*: this plot indicates a positive correlation between the outflow mass loading factor ($\dot{M}_{\rm H_2,OF}/SFR$) and $L_{\rm AGN}/L_{\rm Bol}$ that emerges from the diagram in the left panel. (Fig. 8 of Cicone et al. 2014)

1.2.2 Molecular outflows

Winds and feedback often occur in the form of molecular outflows that carry large amounts of cold molecular gas out from the centre of galaxies. A large fraction of ULIRGs are observed to have wide angle molecular outflows that are detectable using the median velocities of far-infrared OH absorptions (Veilleux et al. 2013). It is believed that these outflows help to regulate the growth of galaxy nuclei. A large fraction of the gas mass in outflows may reside in molecular (H_2) clouds. Indeed, molecular line studies have delivered very high H_2 mass-loss rates of several 100 $M_\odot$ yr^{-1} (Cicone et al. 2014, also Fig. 1.3), which may therefore have a large impact on the star formation in the host galaxy.

Since molecular outflows may evict significant masses of gas out of the galaxy, or the gas may return to the system to fuel another growth spur (e.g. Aalto et al. 2020), they are important to our understanding and modelling of galaxy evolution. There has been a discussion of the origin of the molecular gas in the outflows: is it carried out in molecular form from the disk and nucleus, or is it formed in situ in the outflow through instabilities in the hot gas? For the latter possibility, one proposed scenario of molecules forming in outflows is presented in Richings & Faucher-Giguère (2018).This will be discussed further in Chapter 3.

Energy sources

Here I describe a rough structure of the physical processes related to the galactic outflows. Possible energy sources for the molecular outflows are starburst or AGN.

There are several stellar processes which inject mass, momentum and energy into the

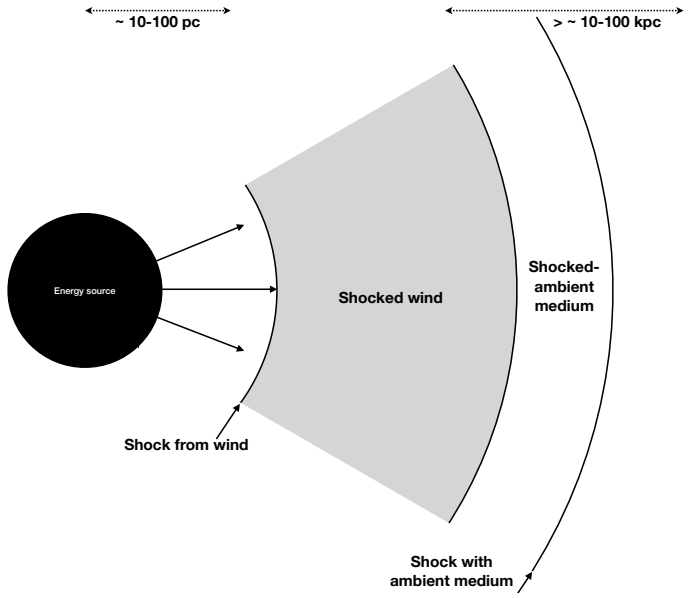

Figure 1.4: A schematic drawing of outflow driving mechanism (adapted from Faucher-Giguère & Quataert (2012)).

surrounding environment, which may affect the rate of star formation. The most important processes are supernova (SN) and hot stellar winds from young massive stars. When a star with a mass over 8 $M_\odot$ ends its life, its core collapses and ejects a large par of its mass with kinetic energy $E_{\rm SN} \simeq 10^{51}[\rm erg] \equiv E_{51}$ and momentum $p_{\rm SN} = \sqrt{2E_{\rm SN}M_{\rm SN}}$, where $M_{\rm SN}$ is the mass of the ejected material per SN. Supernovae are broadly classified into core-collapse types (II, Ib, Ic) originating from massive stars, and thermonuclear type Ia, which result from white dwarfs in binary systems. Other stellar processes include protostellar outflows, type Ia supernovae, and stellar winds from old stars, which seem not play an important role in driving the cool outflows in starburst and active galaxies.

In the case of an AGN, the primary energy source to drive outflows is accretion onto the central SMBH. The gravitational potential energy released by the accreted material is transformed into thermal energy and partly to radiation.

There are two modes in AGN feedback: *radiative* and *kinetic*, depending on the accretion rates. The radiatively efficient AGN gives feedback in "radiative" (or "quasar") mode. This type of AGN has a high accretion rate, and the feedback can often be seen as wide-angle outflow. A radiatively inefficient AGN gives feedback in "kinetic" or "radio" mode. This type of AGN has a lower accretion rate, which gives rise to radio jets.

Driving mechanisms

Both starbursts and AGNs can exert their energy into the surrounding medium in multiple forms. The radiation from the central energy source can create a pressure to push the immediate surroundings outwards. The kinetic energy can directly push the medium as well. It also heats up the medium to create hot winds. Cosmic rays can also contribute to

move the gas outwards. Furthermore, AGNs can also carry the ambient medium through jet entrainment.

Molecular outflows may be *energy-driven* when radiative losses are negligible, or *momentum-driven* when radiative losses are not negligible. They are difficult to distinguish observationally because often both mechanisms are at work.

Fig. 1.4 is a simple sketch to explain the impact given from the energy sources to the ambient medium. The central energy source, an starburst or an AGN (or both of them) drives a wind from the surface of the region. The small scale wind experiences a wind shock with the immediate surrounding medium and the bulk kinetic energy of the wind is converted into thermal energy. The thermal energy inflates a bubble of very hot gas which can push the interstellar medium in the galaxy outwards. The swept up gas will pile up and be observed in molecules with an area of a few kiloparsec, which drives a second shock at the outer radius with the ambient medium.

Whether a large-scale outflow is energy-driven or momentum-driven depends on the conditions of the hot bubble region (the grey-coloured region in Fig. 1.4). If the cooling time in the hot bubble is shorter than the time it takes for the wind to expand in the galaxy, it loses its support of thermal pressure, and the momentum of the gas that was swept up at the outer edges is basically just what was put in by the central engine. On the other hand, if the gas in the hot bubble remains hot, the thermal energy is trapped and can be used to do work on the swept up ambient medium. That work can give momentum to the swept up gas, thus can be said, energy-driven.

If the outflow is energy-driven, the energy injected in the ambient gas (thermal energy, $E_{\rm th}$) is transformed into the kinetic energy ($E_{\rm kin}$) of bulk motion at a rate $\dot{E}$, which is proportional to $\dot{M}v_{\rm out}^2$. Whilst if the outflow is momentum-driven, the energy injected in the ambient gas is due to the momentum that was put in by the central energy source, thus $\dot{E} \propto \dot{M}v_{\rm out}$. Therefore, Murray, Quataert, & Thompson (2005) argued that estimating the mass loss rate of outflows is a way to distinguish between the two driving mechanisms.

Tracers and observations of molecular outflows are discussed further in chapter 3.

1.3 This Thesis

This thesis aims to address the physical and chemical properties of dense molecular gas in the nuclei of Luminous Infrared Galaxies (LIRGs), using hydrogen sulphide (H_2S) as a diagnostic tool. Through detailed observations, it reveals complex gas dynamics including inflow, outflow, and potential counter-rotation, in dust-obscured galactic centres. The research demonstrates that H_2S is often enhanced in regions affected by shocks and feedback from intense star formation or active galactic nuclei. While important advances are made in connecting nuclear gas reservoirs and outflow activity, remaining questions include the exact processes responsible for H_2S enhancement, the nature and fate of dense outflowing gas, and the long-term impact on galaxy evolution. As a whole, this work contributes new insights into the hidden mechanisms making active galaxies active, and highlights the value of multi-molecule, high-resolution studies for probing feedback and molecular evolution.

CHAPTER 2

Molecular Lines

General references: Veilleux et al. (2020), Solomon & Vanden Bout (2005)

(U)LIRGs are rich in molecular gas, which feeds star formation and AGN activity. Several observations have shown that (U)LIRGs also often have molecular outflows. Tracer molecules are required to probe the mass, dynamics and distribution of the molecular gas. Millimetre and sub-millimetre wave techniques can provide direct estimates of the luminosity, kinematics, and morphology of the molecular emission. This information can be converted into estimates of the physical properties of the molecular clouds, for example column- and volume density, mass, momentum and energy. There are a large number of molecular transitions in the millimetre/sub-millimetre-wave window. This means that observations provide a unique view of the chemistry and excitation in the outflowing gas.

To investigate the energy source and driving mechanism of molecular outflows in galaxies, we need a combination of molecules that trace the full extent of the outflow, from its launch point and out to its outer edge. These molecules should have transitions that are excited in such a way that we can locate where the emission comes from. Molecular line emission (and continuum) is also important to probe the central rotating discs of dusty galaxies to determine physical conditions,dynamics and enclosed mass.

But, some of the (U)LIRGs (for example CONs) are so dusty and dense in their central region that traditional tracers of dense gas (such as HCN and HCO^+) can not penetrate to reach telescopes. It is therefore important to explore more tracers that go beyond the standard ones.

2.1 Brightness temperature, flux density and luminosity

Measurements obtained with single-dish radio telescopes are usually expressed in Rayleigh-Jeans brightness temperature units of Kelvins, corresponding to $T_{\rm B} = I_\nu c^2/2k\nu^2$, where I_ν is the specific intensity, k is the Boltzmann constant and ν is the frequency of the line. In interferometers, the measurements are usually expressed in flux density units. The conversion between temperature surface brightness units and flux density is

$$T_{\rm B} = 1360 \frac{\lambda^2}{\theta^2} S_\nu[K], \tag{2.1}$$

where $T_{\rm B}$ is the Rayleigh-Jeans brightness temperature in K, θ is the full-width at half-maximum of the Gaussian beam of the observation in arcseconds, λ is the wavelength of the observation in cm, and S_ν is the flux density in Jy beam^{-1}. The Rayleigh Jeans brightness temperature can be expressed with the excitation temperature of the transition through

$$T_{\rm B} = \frac{h\nu}{k} \left(1 - {\rm e}^{\tau_{\rm J}}\right) \left(\frac{1}{{\rm e}^{\frac{{\rm h}\nu}{{\rm k}T_{\rm ex,J}}} - 1} - \frac{1}{{\rm e}^{\frac{{\rm h}\nu}{{\rm k}T_{\rm cmb}}} - 1} \right), \tag{2.2}$$

where the cosmic microwave background temperature $T_{\rm cmb}$ is the background against which the emission is measured and J is the upper-level of the transition. The last term is usually a small correction for $z \sim 0$, and it is frequently neglected.

Luminosities are frequently expressed in units of K km s^{-1} pc^2, and when using these units they may be noted as L'. In general,

$$L'_{\rm line} = 3.25 \times 10^7 S_\nu \Delta v \nu_{\rm obs}^{-2} \left(1+z\right)^{-3} D_{\rm L}^2, \tag{2.3}$$

where S_ν is the flux density in Jy, Δv is the line width in km s^{-1}, $\nu_{\rm obs}$ is the observed frequency in GHz, z is the source redshift, and $D_{\rm L}$ is its luminosity distance in Megaparsec (Solomon & Vanden Bout 2005).

2.2 CO as reservoir tracer

Over a very wide variety of conditions, the brightest transitions from molecular gas at millimetre/sub-millimetre wavelengths are the rotational transitions of carbon monoxide (CO), ^{12}C^{16}O. These transitions of CO are excited mostly through collisions with H_2 molecules. Radiative trapping will play an important role in the excitation if the transition is optically thick, which is easy to achieve since CO is an abundant molecule that is frequently the largest reservoir of carbon in the gas phase. CO is also the most abundant molecule after H_2, and X(CO) may reach 10^{-4} (in relation to H_2). The low-J transitions of CO mainly trace the bulk of the gas including more diffuse (unbound) phases. Low-J CO line emission probes different gas conditions than the dense gas tracers trace. The critical density of CO J=1-0 can be as low as $n_{\rm crit} \sim 10^2$ cm^{-3} (see below), and it can probe gas with relatively low number density.

CO emission lines are used to calculate the molecular mass because it is the next abundant molecule in the clouds, including in outflows. The observed CO luminosity is converted to the molecular mass using a CO-to-H_2 conversion factor, $\alpha_{\rm CO}$. There is a continuing discussion on this factor, though, since this includes assumptions on cloud physical conditions and self-gravitation that are often difficult to verify. For example, the CO luminosity depends on the optical depth effects, including kinematics and excitation temperature, of the emitting molecular gas which introduces non-trivial effects on the conversion of the line luminosity to the molecular gas mass (see for example the discussion in Veilleux et al. (2020)). Cicone et al. (2018) used an alternative method to estimate the molecular mass of the outflow of NGC 6240, using the neutral atomic carbon fine-structure line [C II] $^3P_1 - ^3P_0$ 492 GHz .

2.3 Dense molecular gas and HCN, HCO^+

HCN is one of the most abundant H_2 mass tracers after CO. HCN J=1-0 line emission traces molecular gas at densities $n_{\rm H_2} \gtrsim 3 \times 10^5$ cm^{-3} which is three orders of magnitude higher than CO J=1-0 (Gao & Solomon 2004a).

HCN has a high dipole moment (μ = 2.98 D for HCN) compared to that of CO (μ = 0.11 D for CO), which makes its lower transitions excellent tracers of dense molecular gas in galaxies. This is because critical densities of rotational transitions are proportional to the square of the dipole moment, $n_{\rm crit} \propto \mu^2 \nu^3_{\rm J+1J}$ (for optically thin lines at frequency $\nu_{\rm J+1J}$) (Papadopoulos 2007), and the excitation is such that bright emission usually requires densities that are similar to or larger than $n_{\rm crit}$. Critical densities of HCN 1–0 and CO 1–0 emission lines, for example, are calculated $\sim 10^5$ cm^{-3} and $\sim 10^2$ cm^{-3}, respectively at T = 50 K. HCO^+ rotational lines are also considered as a dense gas mass tracer due to the same reason, i.e. high dipole moment (μ_{10} = 3.92 D for HCO^+) leading to its higher critical density ($n_{\rm crit} \sim 10^4$ cm^{-3} at T = 50 K).

A HCN molecular line intensity is the results of the excitation and/or its abundance. HCN can be excited either collisionally or being pumped by infrared continuum. The collisional excitation is affected by the abundance, which may be enhanced by high temperature and shock chemistry. On the other hand, HCO^+ abundance is less affected by shocks (Tafalla et al. 2010), therefore it is valuable to obtain both dense gas tracers.

Line intensity ratios of those dense gas tracers to CO (such as HCN/CO and HCO^+/CO), are employed as, to first order, indicators of density, or dense gas content. However comparison among molecular species can be affected by their relative abundances which are determined by the chemistry. There can be more than one collisional partner to excite some molecules. For example, HCN and HCO^+ have a 10^5 and a 10^4 times larger cross-section to collisions with electrons than with hydrogen molecules, respectively. This may affect their use as density tracers in regions where electrons are abundant (Goldsmith & Kauffmann 2017). More importantly, infrared radiative excitation and pumping may affect those molecules, which can impact the interpretation of the rotational transition molecular line emission.

In general the presence of bright emission from one of the high-dipole moment species like HCN or HCO^+ is taken to suggest that the volume density is similar to or higher than the critical density of the transition. A full treatment of the gas density requires solving the detailed balance equation to establish the population of each rotational level. This can

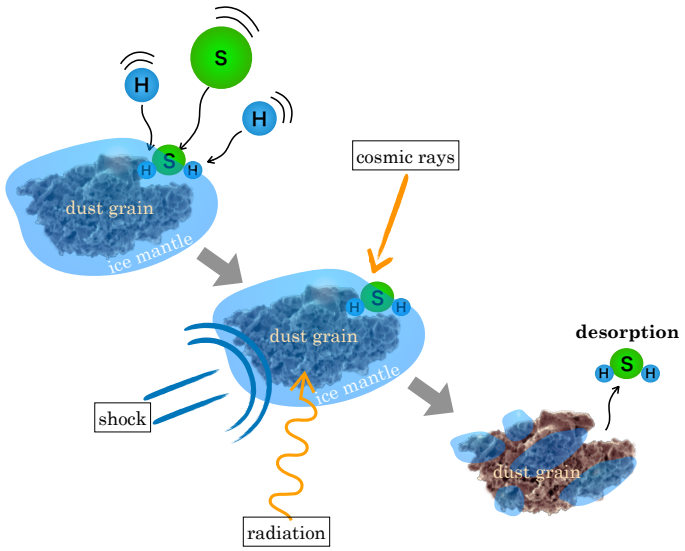

Figure 2.1: Schematic picture on the formation and desorption of H_2S molecule. (Credit:D.Tafoya)

provide simultaneous constraints on volume density, column density, and temperature.

However, in the extremely dense regions of CONs, even the emission from those traditional dense gas tracers can not escape. This is because the large opacities and temperature gradients give rise to effects of self-absorption in the line emission. The molecules also absorb continuum emission from the nuclear dust source. As briefly mentioned in Sect.1.1.2, the HCN-vib emission line can be used in those cases.

2.4 H_2S

Sulphur (S) is one of the most abundant elements in the universe. However, the abundances of sulphur-bearing species derived from observations are much lower than expected in the ISM. The observed low abundances are thought to be mainly due to depletion inside molecular clouds during the cold collapse phase. While it is expected that most sulphur-bearing molecules in dense cores are locked on the ice mantle around grains, they can be released into the gas phase in hot cores or in the regions affected by strong shocks. However, even in the Orion KL hot core (T = $\sim$ 100-300 K), the observed H_2S fluxes (Wakelam et al. 2004) can be best reproduced with an initial sulphur abundance of 0.1 times the sulphur solar abundance, suggesting that 90 % of the sulphur solar abundance has been depleted (Crockett et al. 2014; Esplugues et al. 2014).

Depleted sulphur may form sulphur-bearing molecules, which are subsequently released into the gas phase through desorption from icy grain mantles via several mechanisms. Most sulphur locked in ice mantles is incorporated into hydrogen sulphide (H_2S), making it a primary sulphur reservoir of particular interest to astrochemists (Charnley 1997; Viti et al.

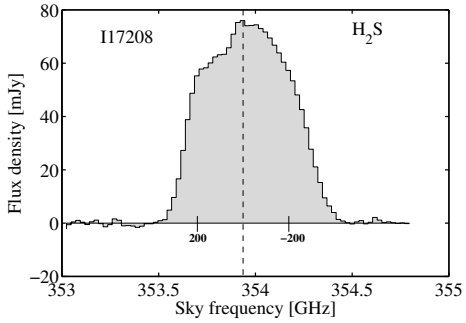

Figure 2.2: ALMA H_2S spectrum of the Galaxy IRAS 17208-0014. The x axis is sky frequency in GHz. The velocity relative to the systemic velocity of IRAS17208-0041 (cz =12 834 km s^{-1}) is shown in the axis at Flux Density = 0 mJy.

2004; Wakelam et al. 2004). H_2S forms through sulphur atom hydrogenation on grain surfaces, followed by desorption via: (i) thermal processes (shocks or infrared radiation), (ii) UV photodesorption, (iii) cosmic-ray-induced desorption, or (iv) shock sputtering (Fig.2.1, Sato et al. 2022, and references therein). Chemical desorption may also contribute significantly under certain conditions (Navarro-Almaida et al. 2020a; Oba et al. 2019), though its efficiency diminishes at densities above 2×10^4 cm^{-3} in cold (∼10 K), high-extinction environments (Navarro-Almaida et al. 2020b; Vidal et al. 2017). Gas-phase hydrogenation becomes viable at kinetic temperatures exceeding several thousand Kelvin (Mitchell 1984).

The detection of H_2S line emission indicates substantial gas-phase abundances, first observed in Milky Way dark clouds (Thaddeus et al. 1972) and later in Galactic sources such as outflows and hot cores (Herpin et al. 2009; Minh et al. 1990; Navarro-Almaida et al. 2020a). Enhanced H_2S abundances ($X_{H_2S} \sim 10^{-6}$) in outflow-affected regions (Minh et al. 1990) align with shock models requiring velocities >25 km s^{-1}, densities $>10^5$ cm^{-3}, and weak magnetic fields (Pineau-desForets et al. 1993). These conditions suggest shock-induced thermal desorption as a key mechanism, though alternative processes must operate where shocks are absent.

Radiation from nuclear starbursts or active galactic nuclei (AGN) can thermally desorb H_2S by elevating dust temperatures (Bachiller et al. 2001; Charnley 1997; Hatchell & Viti 2002; Minh et al. 1990, 2007; Woods et al. 2015). In cooler environments (10–50 K), photodesorption by secondary UV fields may dominate (Goicoechea et al. 2021). Shock waves additionally contribute through gas compression and heating: C-type shocks desorb molecules without full dissociation (Holdship et al. 2017), while extreme J-type shocks (>80 km s^{-1}) destroy H_2S (Neufeld & Dalgarno 1989). Observational evidence for shocks includes broad H_2S line wings in spectral profiles.

Determining the dominant desorption mechanism requires constraining local physical conditions. Kinetic temperatures and densities derived from H_2S line ratios can discriminate between radiation-driven, shock-induced, or alternative desorption pathways, providing critical insights into sulphur chemistry evolution in diverse astrophysical environments.

The first extragalactic detection was reported in 1999 towards the Large Magellanic Cloud (LMC) (Heikkilä, Johansson, & Olofsson 1999). There were three more extragalactic detections before my work that I report here, toward NGC 253 (e.g. Martin et al. 2005), Arp 220

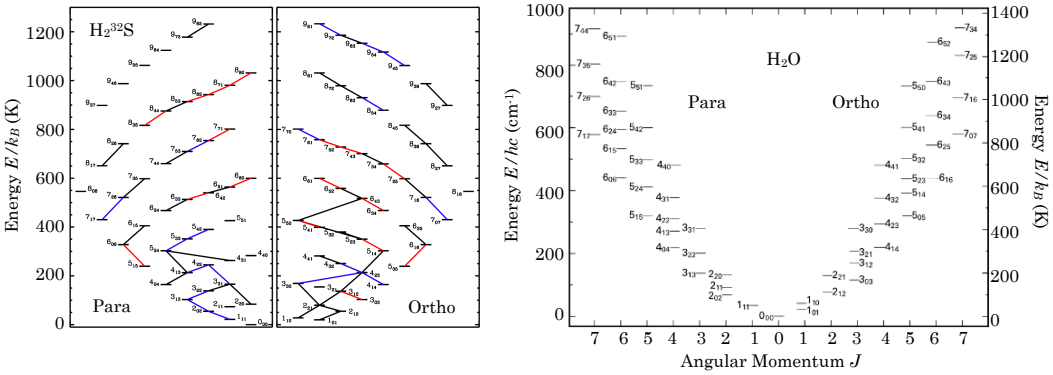

Figure 2.3: Energy-level diagrams of $H_2^{32}S$ (*left*, Crockett et al. (2014)) and H_2O (*right*, Banzatti (2013)).

(e.g. Martín et al. 2011), and IRAS17208-0014 (Aalto et al. 2015b). Aalto et al. (2015b) detected strong higher transition line of H_2S toward IRAS17208-0014 (Fig.2.2). There are two lines (ortho-H_2S $3_{2,1}$–$3_{1,2}$ and para-H_2S $4_{3,1}$–$4_{2,2}$) at 369 GHz with only 26 MHz between them, so the lines are blended into one line. They discussed that H_2S might be generated in relation to the energetic activities like outflows, starbursts in dense gas.

Another importance of H_2S molecule comes from its chemical similarity to the water molecule (Fig.2.3). This leads to both of them having similar formation processes including grain chemistry processes. From the above discussion, H_2S may serve both as a shock tracer and a water proxy. The benefit of H_2S compared to H_2O is that its ground-state line is observable by ground-based telescopes for nearby galaxies. We have a discussion in relation to this in my paper I.

CHAPTER 3

Molecular probes of outflows

3.1 CO

Molecular outflows in dusty galaxies may be detected in absorption in far-infrared transitions of OH (see Veilleux et al. 2020, for a review), but to get the full extent and morphology it is important to image the outflows. The most common molecular line used for this is the J=1-0 transition of CO.

Following the first extragalactic detection by Nakai et al. (1987), toward the luminous starburst galaxy M 82, CO emission has been detected in many more starburst galaxies - for example NGC 2146, NGC 1808, NGC 3628, VII Zw 31, NGC 1614, NGC 3256 (Fig. 3.1), ESO 320-G 030, and NGC 4945 (e.g. García-Burillo et al. 2015; Henkel et al. 2018; Leroy et al. 2015; Pereira-Santaella et al. 2016; Sakamoto et al. 2014; Salak et al. 2016; Tsai et al. 2009, 2012).

AGN galaxies with known CO outflows include Mrk 231, M 51, IRAS 13120, IRAS 17208-0014, NGC 1433, NGC 1068, IC 5063, Circinus, Mrk 273, NGC 1266 and NGC 1377 (e.g. Aalto et al. 2012; Aalto et al. 2016, 2017, 2020; Aalto 2012; Aladro et al. 2018; Alatalo et al. 2011; Alatalo 2015; Cicone et al. 2012; Combes et al. 2014; Dasyra et al. 2016; Feruglio et al. 2010; García-Burillo et al. 2014; Matsushita et al. 2015; Morganti et al. 2015; Oosterloo et al. 2017; Privon et al. 2017; Zschaechner et al. 2016). There are also galaxies that experience a combined AGN- and SB-driven outflow, for example NGC 6240 (Feruglio et al. 2013; Saito et al. 2018).

The low-J CO line may trace the full extent of the outflow, that shows a variety of morphology, and is often used as a tracer of molecular mass (See, Sect.2.2).

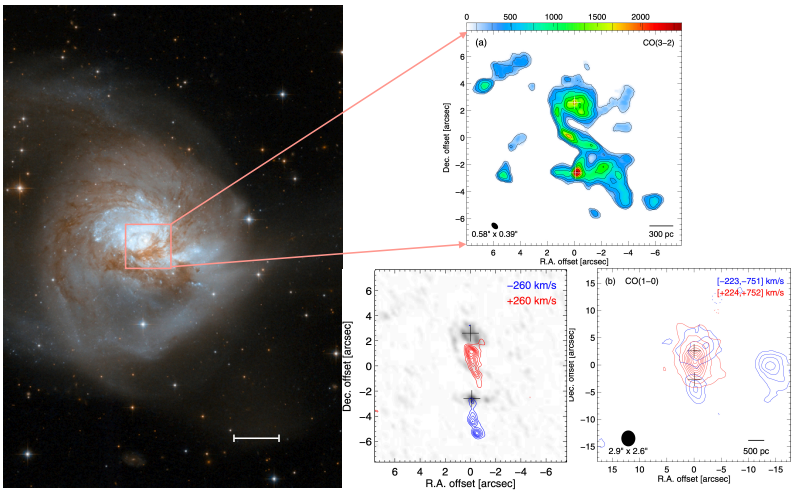

Figure 3.1: Molecular outflow traced by CO at NGC 3256. *Top*: CO(3-2) moment 0 map. *Bottom left*: CO(3-2) channel map of high-velocity emission at 0".5 resolutions. *Bottom right*:CO(1-0) map of high-velocity emission at around 3" resolution. (Sakamoto et al. 2014). *left*: HST image of NGC 3256 (NASA/ESA/A.Evans).

3.2 HCN, HCO^+, CN

It is often found that emission from dense gas molecular tracers (such as HCN and HCO^+ which trace $n_{H_2} \gtrsim 3 \times 10^4$ cm^{-3}, or CN ($n_{H_2} \gtrsim 1 \times 10^6$ cm^{-3})) are enhanced in galactic outflows (e.g. Aalto et al. 2015a; Aalto 2012; Barcos-Muñoz et al. 2018; Cicone et al. 2020; Falstad et al. 2018; García-Burillo et al. 2014; Harada et al. 2018; Impellizzeri et al. 2019; Michiyama et al. 2018; Walter et al. 2017). Lindberg et al. (2016) studied the outflow features in the HCN, HCO^+ and HNC emission lines in Mrk 231 and discussed the velocity structure in terms of shocks in the outflow (Fig.3.2). Cicone et al. (2020) found extremely luminous CN emission in the same outflow and studied this in terms of UV irradiation and star formation.

It is possible that the higher compression of the gas in some outflows makes the dense phase of the molecular gas more prevalent than in galactic discs of the host galaxy, or the diffuse molecular phase is more easily evaporated and destroyed, or probably both phenomena are at work. Studying the dense gas phase in the outflow - using a combination of tracers - is key to the understanding of the physical conditions and evolution of the outflow, and how it relates to the driving mechanism of the outflow and the properties of the host galaxy.

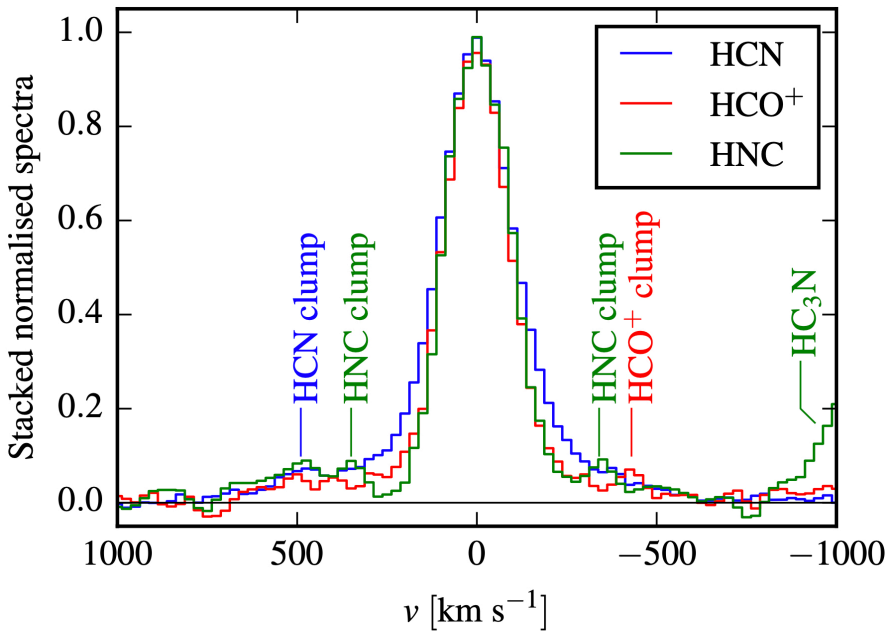

Figure 3.2: HCN 1–0, 2–1, and 3–2 lines; the HCO^+ 1–0 and 2–1 lines; and the HNC 1–0 line of Mrk 231 observed with IRAM PdBI, are shown normalised, rigridded, and stacked weighted by the S/N to show the variations in line profile between the species. (Lindberg et al. 2016)

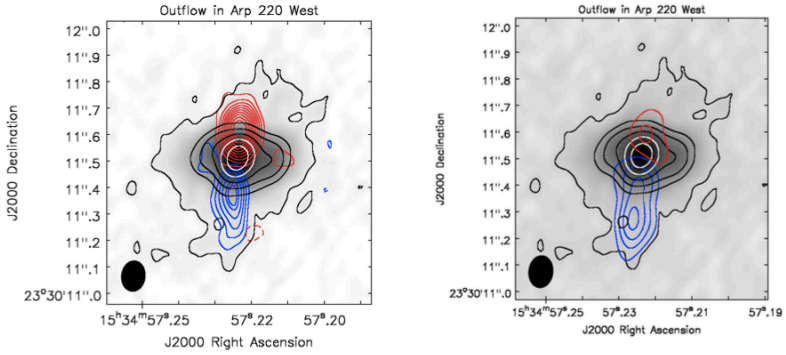

Figure 3.3: HCN (1-0) (left) and CO (1-0) (right) emission of the integrated intensity map are shown in red- and blue contours for redshifted and blueshifted channels, respectively. Greyscale: 92 GHz continuum image of the western nucleus of Arp 220 with its black (3,24,48 and 96 $\times\sigma_{92\mathrm{GHz}}$) and white (192, 384$\times\sigma_{92\mathrm{GHz}}$) contours. (Fig.3 of Barcos-Muñoz et al. 2018)

3.3 Outflows from CONs

As discussed in Sect.1.1, molecular outflows are seen in (U)LIRGs that are CON-hosts. These outflows are not obvious in the far-infrared OH lines (see Falstad et al. 2019, for a discussion), but can be detected at mm-wavelengths in for example CO or HCN emission. Barcos-Muñoz et al. (2018) reported a fast molecular outflow detected in HCN (Fig.3.3). Other examples include an outflow detected in the cm-wave OH-line in the LIRG Zw 049.057 (Falstad et al. 2018), a fast CO-outflow in the ULIRG-CON IRAS17208-0014 by García-Burillo et al. (2014), and nuclear feedback in the LIRG-CON IC 860 (Aalto et al. 2019). In CONs, both in- and outflows seem to be occurring at the same time (Falstad et al. 2021).

3.4 Origin of the H_2

The origin and the fate of the molecular gas in the galactic outflows are still not well understood. One question is whether the gas was formed in the host galaxy and has being swept up from its circumnuclear disc, or it is formed in the outflow from the precursory atoms, ions or molecules (e.g. Ferrara & Scannapieco 2016; Richings & Faucher-Giguère 2018). Another question is whether the molecular gas in the outflow spreads and evaporates, or whether it condenses to form stars (Maiolino et al. 2017). It is also poorly known what fraction of the gas is expelled from the galaxy by the driving force of the outflow, and what fraction returns to fuel another cycle of activity in the same galaxy (e.g. Lutz et al. 2020; Pereira-Santaella et al. 2018).

A good estimate of the molecular mass is critical for the questions above, but it is also a challenge to determine the mass. Molecular hydrogen, H_2, is the most abundant ($\sim$ 99%) molecule but typically is not observed [1]. One of the reasons is that it has no permanent

[1] Richings & Faucher-Giguère (2018) suggested in their simulations that most H_2 is warm and observable in infrared rotational lines in outflows. This might explain the warm H_2

electric dipole moment, meaning the transitions tends to be relatively weak in emission. Another reason is that the temperature of the typical galactic molecular clouds are lower than that necessary to excite H_2 rotationally ($T_{\rm min} = 510$ K $\gg T_{\rm GMC}$). Instead, CO emission lines are used to calculate the molecular mass (see sect.2.2 for a brief discussion on this.).

excess found by Spitzer in ULIRGs (Hil & Zakamska 2014)

CHAPTER 4

Observations and data reduction

The molecular lines discussed in this thesis are found in the mm-submm range (0.4 - 1.8 mm). To detect the signal from our targets within a reasonable time (tens of hours) and to distinguish the emission's angular location, we require radio telescopes whose aperture (and, for interferometers, baselines) provides sufficient sensitivity and angular resolution at the molecular-line wavelength.

4.1 Telescopes

There are two types of radio telescope for detecting the molecular line emissions in the mm-submm range: a single-dish telescope which is typically a parabolic reflector and an interferometer which is composed of multiple parabolic antennae.

4.1.1 Single-dish telescopes

A single-dish radio telescope (typically a parabolic reflector) operates as a single aperture, in contrast to an interferometer, which combines multiple antennas observing simultaneously toward the same target. The angular resolution of a single-dish telescope scales with wavelength and aperture as $\theta \sim \lambda/D$. The sensitivity depends on the effective collecting area ($A_{\rm eff} \propto D^2$), the total on-source time t, and the spectral resolution (channel width) $\Delta\nu$ where noise scales roughly as $\sigma \propto 1/\sqrt{\Delta\nu\, t}$.

The radio/millimetre emission collected by the dish is brought to focus and coupled via a feed horn to the receiver, where it is converted to an electrical signal for detection and

recording. The optics (primary and, if present, subreflector) form the beam and feed a corrugated horn; an OMT/polariser separates the desired polarisation(s). A cryogenic low-noise receiver amplifies the signal and, using a mixer driven by a stable local oscillator, down-converts the sky frequency to an intermediate frequency (IF). Band-defining filters and levelling ensure a flat, well-conditioned IF.

4.1.2 Interferometers

General reference: Alma Cycle 12 Technical Handbook [1]

The angular resolution of a single-dish telescope is fundamentally limited by diffraction, with the Half Power Beam Width (HPBW) given by $1.02\,\lambda/D$ for a uniformly illuminated circular aperture of diameter D. As a result, even at millimetre wavelengths where the wavelength λ is relatively small and the angular resolution is therefore at its best for radio observations, the resolution of single-dish telescopes remains orders of magnitude worse than that of optical telescopes.

To overcome this limitation, radio astronomers use interferometry. Interferometry allows radio telescopes to achieve high angular resolution by combining the signals received by multiple antennas. Each antenna pair samples a specific spatial frequency of the sky brightness distribution, with the measured signal represented as a complex quantity known as a *visibility*. The full set of visibilities encodes both amplitude and phase information across spatial frequencies, enabling image reconstruction through Fourier inversion. The accuracy and fidelity of the resulting image depend critically on the completeness of the spatial frequency coverage, i.e., how well the relevant angular scales are sampled.

For an array, replace D by the *maximum baseline* $B_{\max}$: the angular resolution is $\theta \sim \lambda/B_{\max}$. Point-source sensitivity improves with total collecting area and the number of antenna pairs; a common scaling is

$$\sigma_S \propto \frac{1}{\sqrt{N_{\text{ant}}(N_{\text{ant}}-1)\,\Delta\nu\,t}}$$

for identical antennas and natural weighting. The field of view is still set by each dish's primary beam ($\sim \lambda/D$), and emission smoother than the scale set by the *shortest* baseline $B_{\min}$ is filtered out (largest recoverable scale $\sim \lambda/B_{\min}$).

Aperture Synthesis and Complex Visibilities

As mentioned above, in an interferometric array, each pair of antennas measures a cross-correlation of their received signals, $\langle V_1 V_2 \rangle$, which samples a specific spatial frequency in the sky's brightness distribution. The principle is illustrated in the schematic of Fig. 4.1.

The visibility function $\mathcal{V}(u, v)$ - also known as the spatial coherence function - is derived from the cross-correlation of the signals received by a pair of antennas, as measured by the correlator. The coordinates (u, v) represent the components of the projected baseline vector expressed in units of the observed wavelength. That is the separation between the antennas

[1] `https://almascience.eso.org/documents-and-tools/cycle12/alma-technical-handbook`

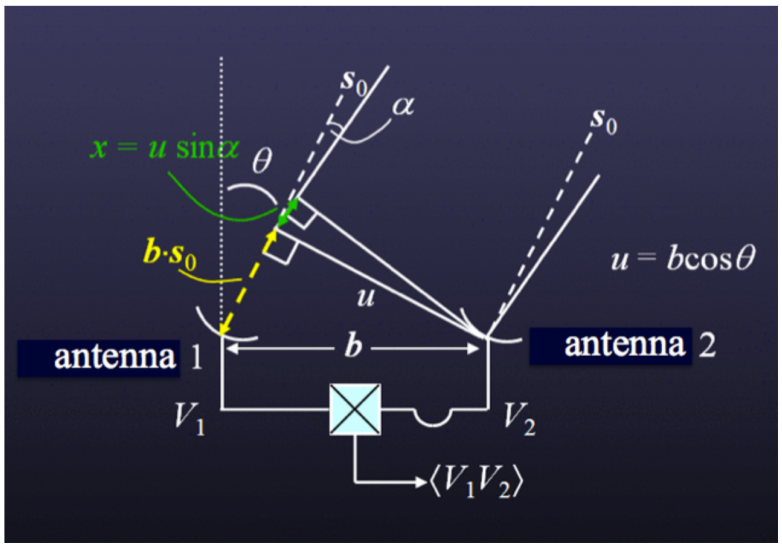

Figure 4.1: An ideal 1-D interferometer consisting of two antennas, 1 and 2, separated by a baseline b. Both are pointed toward a sky location at angle θ; the projected distance in that direction is $u = b\cos\theta$. The correlator combines the voltages detected from each antenna and produces a cross-correlation $\langle V_1 V_2 \rangle$.

projected onto the plane perpendicular to the direction of the source.

According to the van Cittert–Zernike theorem, the visibility function is related to the sky brightness distribution $I(l, m)$ via a two-dimensional Fourier transform:

$$\mathcal{V}(u, v) = \iint I(l, m)\, e^{-2\pi i(ul+vm)}\, dl\, dm,$$

where l and m are the direction cosines of the source relative to the phase tracking centre.

This fundamental relationship enables the reconstruction of the sky brightness distribution from the measured visibilities, provided there is sufficient sampling in the (u, v)-plane. By observing with multiple antenna pairs and taking advantage of Earth's rotation, an interferometric array samples a range of spatial frequencies corresponding to different points in the (u, v)-plane. The denser and more uniform this coverage, the more accurately the sky intensity distribution can be reconstructed, leading to higher image fidelity.

4.1.3 Telescopes used for this thesis

In the following, I describe the observational instruments used to acquire the data analysed in this thesis.

Figure 4.2: Some pictures of APEX telescope at Chajnantor plateau, Chile. (Photo credit: *left*:D.Tafoya, *right-bottom*: R.Unnikrishnan)

Atacama PathFinder EXperiment (APEX, single-dish telescope)

General reference: APEX Calibration and Data Reduction Manual[2]

The APEX telescope has been used to obtain some of the observational data in this thesis (Fig.4.2).

APEX started as a collaboration between the Max-Planck-Institut für Radioastronomie (MPIfR), the Onsala Space Observatory (OSO) and the European Southern Observatory (ESO). This millimetre and sub-millimetre observatory is located at the Chajnantor plateau in Chile, which was chosen for its high elevation (around 5000 m above sea level) and low-humidity environment, minimising the effect of water vapour on observations. The dish of the telescope has a diameter of 12 metres, the frequency coverage ranges from 157 GHz to 850 GHz.

One of the receivers is SEPIA180, which covers a frequency range from 159 to 211 GHz (Belitsky et al. 2018). This is suitable to observe the lower transition lines of several molecules including dense gas tracers such as HCN, HCO^+, HNC and other molecules such as CH_3OH, SO, and H_2S. SEPIA180 is a dual polarisation 2SB receiver built to the specifications of ALMA Band 5, which is based on the pre-production version of this receiver. The instrument was built by the Group for Advanced Receiver Development (GARD) at OSO. The SEPIA180 receiver has two IF outputs per polarisation, un upper sideband (USB) and a lower sideband (LSB), each covering 4-8 GHz, adding up a total of 16 GHz instantaneous IF bandwidth. The central frequencies of the two sidebands are separated by 12 GHz. The full width at half maximum (FWHM) beam size of APEX at the SEPIA180 frequencies is in the range of 30 - 39 arcseconds.

[2] `https://www.apex-telescope.org/documents/public/APEX-MPI-MAN-0012.pdf`

IRAM Northern Extended Millimeter Array (NOEMA, Interferometer)

General reference: NOEMA Observing Capabilities and Current Status [3]

The NOEMA is an interferometer undergoing continuous development. Thus here I describe its capabilities as of october 2025. It consists with twelve 15m antennas located on the Plateau de Bure at 2550 m altitude in the French Alps. Powerful dual-polarisation receivers for the 3 mm and 1 mm observing bands were installed in 2006, and extended to the 2 mm observing band in late 2007, and to the 0.8 mm band at the end of 2010. The antennas of the NOEMA interferometer can move on rail tracks up to a maximum separation of currently 1.7 km in the East-West direction and 368 m in the North-South direction, corresponding to a resolution of 0.2 arcseconds at an observing wavelength of 1.3 mm (230 GHz).

Each antenna is equipped with dual sideband receivers with low noise performance and it is possible to observe in three distinct bands. The receivers offer two orthogonal linear polarisations in all bands, with each polarisation offering a simultaneous 7.744 GHz bandwidth in both the lower and upper sidebands.

The wide-band correlator PolyFix offers an instantaneous bandwidth of about 16 GHz, supporting flexible spectral configurations across eight basebands per array. The default spectral resolution is 1.95 MHz throughout the 15.5 GHz effective bandwidth per polarisation. For this low resolution mode, up to sixteen high-resolution *chunks* can be selected in each of the eight basebands. Each of these has a width of 64 MHz and a spectral resolution of 62.5 kHz.

For the observations included in the paper I, the 2 mm band receivers were tuned to 161.934 GHz to cover the H_2S 1_{10}–1_{01} line in the 3.6 GHz bandwidth of the wide-band correlator (WideX).

Atacama Large Millimetre/submillimetre Array (ALMA, Interferometer)

The Atacama Large Millimetre/submillimetre Array (ALMA) is comprised of 66 high-precision antennas on the Chajnantor plateau at 5000 m altitude in Chile (Fig.4.3. The main Array consists of fifty 12-metre antennas for sensitive, high-resolution imaging, complemented by the Atacama Compact Array (ACA), which includes twelve closely spaced 7-metre antennas and four 12-metre antennas for single-dish (Total Power) observations. This configuration allows ALMA to recover emission across a broad range of spatial scales.

The antennas are distributed over 192 stations, with baselines ranging from 15 metres to approximately 16 kilometres, enabling flexible array configurations and a wide range of spatial resolutions. Signals from all antennas are digitised and transmitted via high-speed optical fibres to a central correlator and spectrometer for processing. The ACA addresses the "zero spacing" problem in interferometry by providing short baseline coverage and single-dish data, ensuring high-fidelity imaging of both compact and extended sources.

The ALMA front end accommodates up to ten receiver bands, covering most of the wavelength range from 8.5 to 0.32 mm (35–950 GHz). Each band is designed to match an atmospheric transmission window, as illustrated in Figure 4.4. These windows are shaped by broad absorption features, mainly due to water vapour in the lower atmosphere, and

[3] `https://www.iram.fr/GENERAL/calls/w25/NOEMACapabilities.pdf`

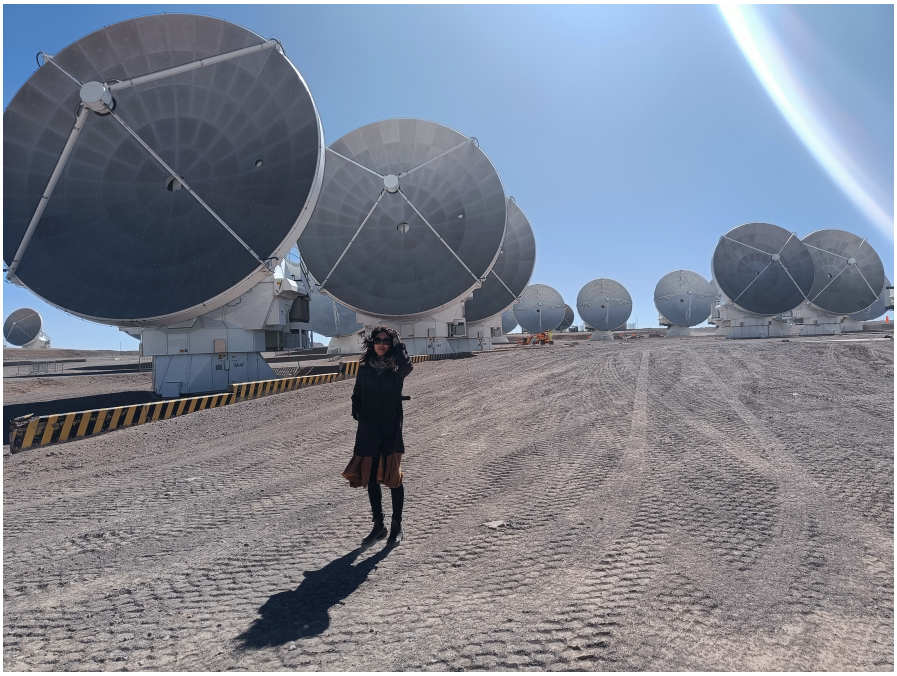

Figure 4.3: The ALMA telescope at Chajnantor plateau, Chile. (Photo credit: R.Unnikrishnan)

narrower features from atmospheric oxygen and ozone.

Here I list a short description about the Band 5, Band 6, and Band 9 receivers below, as I used data taken by these receivers.

- **Band 5 Receiver:** The Band 5 receiver covers 158–211 GHz (1.90–1.42 mm) and is a dual sideband (2SB) design, providing high sensitivity across the 1.7 mm atmospheric window. Notably, Band 5 was developed by the Group for Advanced Receiver Development (GARD) at Onsala Space Observatory, Chalmers University of Technology, Sweden[4]. In this research, H_2S $1_{1,0}$ – $1_{0,1}$ line was detected using this receiver.

- **Band 6 Receiver:** The Band 6 receiver operates from 211–275 GHz (1.42–1.09 mm), also as a dual sideband (2SB) system. It is the most widely used ALMA receiver, covering the 1.3 mm atmospheric window. In this research, H_2S $2_{2,0}$-$2_{1,1}$ was detected using this receiver.

- **Band 9 Receiver:** The Band 9 receiver covers 602–720 GHz (0.50–0.42 mm) and uses a double sideband (DSB) design. Band 9 is highly sensitive to atmospheric conditions, requiring low precipitable water vapour for successful operation. In this project, CO 6-5 line was detected using this receiver.

[4]Belitsky, V. et al., 2018, *Astronomy & Astrophysics*, 611, A98.

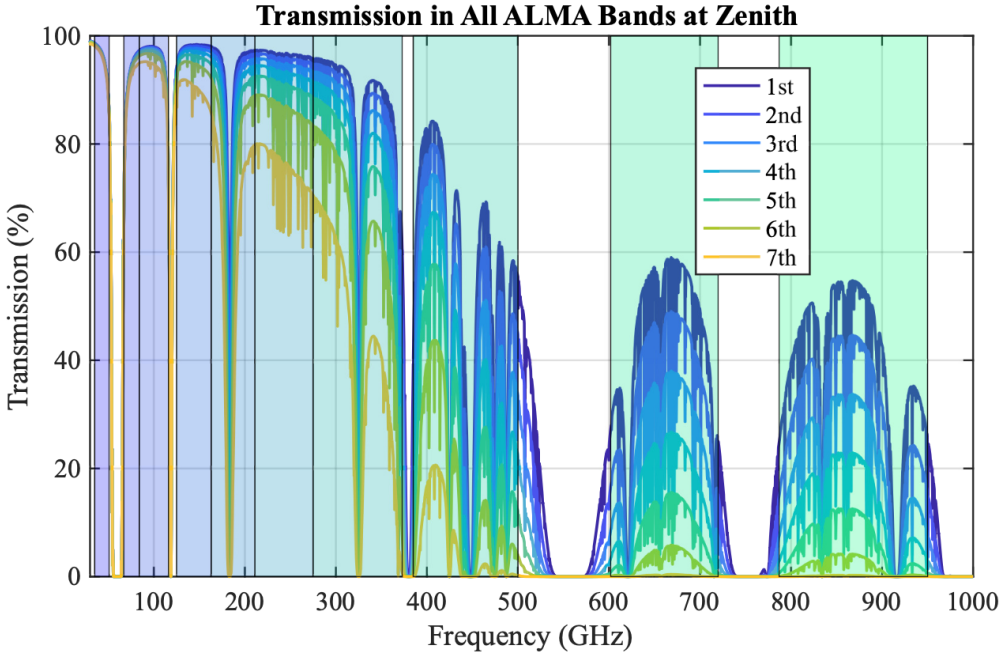

Figure 4.4: The ten ALMA receiver bands (shaded) superimposed on a zenith atmospheric transparency plot at the Array Operation Site (AOS) for the first seven octiles of observing conditions at ALMA.

4.2 Calibrations

The signals from our target sources are affected by instrumental and atmospheric effects, so it is essential to calibrate and correct these to recover the true astronomical signal. In general, errors can be time-dependent and/or frequency-dependent. The former are addressed by gain calibration, while the latter are corrected by bandpass calibration . In addition, a flux calibration sets the absolute intensity scale, converting backend counts, reported in arbitrary power units, into physically meaningful quantities such as antenna temperature (K) or flux density (Jy). These calibrations are required for both single-dish telescopes and interferometers. For interferometers, there is the further requirement of phase calibration: because visibilities are formed from signals received at separate antennas, differential atmospheric and instrumental delays corrupt the relative phase and must be corrected to preserve coherence.

4.2.1 General calibration methods for single-dish telescope

For single-dish telescopes, a calibration signal is injected, either via a switched noise diode or by viewing hot and cold loads, to monitor receiver gain and atmospheric opacity. The intermediate-frequency (IF) output is then digitised: for spectral-line observations it is spectrally channelised by a spectrometer (e.g., FFT or polyphase filter bank), whereas for broadband measurements it is integrated by a total-power radiometer or bolometer.

To convert backend counts to antenna temperature, at least two references of known temperature and measured counts are required to solve for the gain and offset. We use the standard chopper-wheel calibration (Ulich & Haasf 1976), which combines measurements of internal loads and blank sky to set the absolute temperature scale and to correct, across the full bandpass, for atmospheric attenuation and temporal variations in opacity.

The main calibration equation is:

$$T_A^* = T_{\rm cal} \frac{(C_{\rm on} - C_{\rm ref})}{(C_{\rm hot} - C_{\rm sky})} \tag{4.1}$$

where T_A^* is the source antenna temperature after correction, $T_{\rm cal}$ is a calibration factor, and $C_{\rm on}$, $C_{\rm ref}$, $C_{\rm hot}$, $C_{\rm sky}$ are the receiver values for source, reference, hot load, and sky positions.

The process is done in three steps: 1. Subtract the difference between source and reference positions to remove receiver and atmospheric offsets. 2. Adjust the shape of the band and atmosphere using the difference between hot and sky measurements. 3. Set the absolute temperature scale with $T_{\rm cal}$.

The bandpass calibration is typically performed by observing an emission-free region of the sky (an "OFF" position) or by rapidly switching the local oscillator frequency between two closely spaced values ("frequency switching"). Both methods allow the instrumental bandpass shape to be determined and subsequently removed from the on-source spectrum. In position switching, the off position provides a direct measurement of the instrumental and atmospheric baseline, which is subtracted from the on-source data. In frequency switching, the sky signal is modulated in frequency while the instrumental response remains fixed, allowing the bandpass to be characterised without moving the telescope. After demodulation, this process effectively flattens the spectral baseline and corrects for frequency-dependent system gain.

Calibrations summary:APEX

The APEX raw data are stored in the MBFITS data format. For heterodyne observations, these raw data are calibrated online by the apexOnlineCalibrator program, which writes the calibrated spectra (in antenna temperature T_A^* scale) into a CLASS -format data file.

At APEX, calibration uses a slightly different formula from Eq.4.1, adding a normalization factor that takes changes over the bandpass into account:

$$T_A^* = T_{\rm cal} \frac{(C_{\rm on} - C_{\rm ref})/C_{\rm ref}}{(C_{\rm hot} - C_{\rm sky})/C_{\rm sky}} \tag{4.2}$$

For APEX, $T_{\rm cal}$ is usually calculated with a SKY–HOT–COLD load measurement together with the Atmospheric Transmission at Microwaves model (ATM; Pardo, Cernicharo, & Serabyn 2001).

4.2.2 General calibration methods for interferometers

For interferometers, calibration ensures that the measured visibilities between antenna pairs accurately represent the true sky signal by correcting for time-dependent and frequency-dependent instrumental and atmospheric effects.

Temporal & Bandpass Calibration: Antenna-based complex gains are solved as amplitude (A^i) and phase (ϕ^i) terms for each antenna. This allows the calibration to reduce the number of parameters since each baseline gain ($G^{i,j}$) can be written as:

$$G^{i,j} = A^i A^j e^{i(\phi^i - \phi^j)}.$$

Bandpass calibration uses bright continuum sources to correct for frequency-dependent amplitude and phase variations in the receiver or signal chain. It accounts for both dispersive (frequency-dependent) and non-dispersive (delay) effects.

Phase Referencing & Flux Scaling: To maintain phase coherence, phase referencing alternates between the target source and a nearby calibrator. This corrects tropospheric delay and instrumental phase errors by interpolating the calibrator's solutions to the science target. Flux calibration sets the absolute amplitude scale using standard reference sources with well-known flux densities, such as regularly monitored quasars or planetary bodies.

4.3 Imaging

Imaging in radio astronomy is the process of creating spatial maps of objects using radio waves detected by telescopes.

4.3.1 Single-dish telescope imaging

A single-dish telescope detects a signal with one beam, providing a spectrum at each position. To make a spatial map, the telescope observes multiple positions in the sky. Common methods for this are on-the-fly (OTF) mapping and raster scanning. In OTF mapping, the telescope moves continuously across the sky and detects the signal simultaneously, while in raster scanning, the telescope observes in a straight line and then steps over by a set amount to begin the next scan line. The sampled points are placed on a image grid according to their sky coordinates, and a smoothing or weighting (usually Gaussian) is applied to account for the beam shape and sampling intervals. Then the final brightness map is made from convolving the observed sky brightness with the telescope's beam function, which is often of full-width half-maximum (FWHM) proportional to λ/D, where λ is the observed wavelength and D is the diameter of the antenna.

4.3.2 Interferometry imaging

The process of transforming calibrated visibilities into scientifically interpretable images is based on deconvolution and cleaning algorithms, which attempt to correct for both instrumental and sampling artifacts intrinsic to interferometric observations. Due to the finite and discrete sampling of the (u, v) plane, the reconstructed image is referred to as the *dirty image*, and is formed by the convolution of the true sky brightness distribution (weighted by the primary beam response) with the synthesised *dirty beam*, the array's effective point spread function. The sidelobe structure and artifacts in the dirty beam can cause spurious features within the image (see Fig. 4.5).

To recover the intrinsic brightness distribution, the measured visibilities are subject to

inverse Fourier transformation:

$$I(l,m) = \iint \mathcal{V}(u,v) e^{2\pi i(ul+vm)}\, du\, dv, \tag{4.3}$$

where incomplete sampling decides systematic limitations on image fidelity.

Deconvolution, most commonly implemented via the CLEAN algorithm (Cornwell 2009), iteratively models the sky brightness as a collection of point sources. At each iteration, the brightest components are identified and subtracted, convolved with the dirty beam. The outcome is strongly influenced by key parameters such as gain (typically 0.1–0.3), the number of iterations or noise threshold, and the multi-scale treatment for extended emission (Rau & Cornwell 2011). Too much cleaning has a risk of removing faint or diffuse emission, while conservative parameter choices can leave residual sidelobes.

The spatial frequency coverage of the interferometer determines the angular scales accessible in the final image: the finest resolution is set by the longest baselines, $\theta_{\rm res} \approx \lambda/L_{\rm max}$, whereas the largest recoverable scale is set by the shortest baseline, $\theta_{\rm MRS} \approx \lambda/L_{\rm min}$. Consequently, compact array configurations enhance sensitivity to extended structure at the expense of angular resolution, while extended configurations provide higher angular resolution but can resolve out large-scale emission.

Careful configuration planning is necessary for this balance between resolution and sensitivity. Combining data from multiple array setups or integrating single-dish observations are frequent supplemental technique to ensure complete spatial frequency synthesis.

Units and Conversions in Interferometric Imaging

Another way to express the specific intensity or surface brightness of an astronomical source is through the *brightness temperature*, T_B, which is particularly useful in the Rayleigh–Jeans limit. In this regime, the specific intensity is related to T_B by:

$$I_\nu(\theta,\varphi) = \frac{2k\nu^2}{c^2} T_B(\theta,\varphi)$$

Since the flux density S_ν is the integral of the specific intensity over a solid angle, the relationship between brightness temperature and flux density is given by:

$$S_\nu = \iint I_\nu(\theta,\varphi)\, d\Omega = \iint \left(\frac{2k\nu^2}{c^2} T_B(\theta,\varphi) \right) d\Omega.$$

If the brightness temperature is approximately uniform over the source, this simplifies to:

$$S_\nu = \frac{2k\nu^2}{c^2} T_B\, \Omega_s$$

where Ω_s is the solid angle subtended by the source.

For a Gaussian beam and a point-source the conversion between flux density and brightness temperature is:

$$\left(\frac{T}{1\ \mathrm{K}}\right) = \left(\frac{S_\nu}{1\ \mathrm{Jy}}\right) \left[13.6 \left(\frac{300\ \mathrm{GHz}}{\nu}\right)^2 \left(\frac{1''}{\theta_{\rm max}}\right) \left(\frac{1''}{\theta_{\rm min}}\right) \right]$$

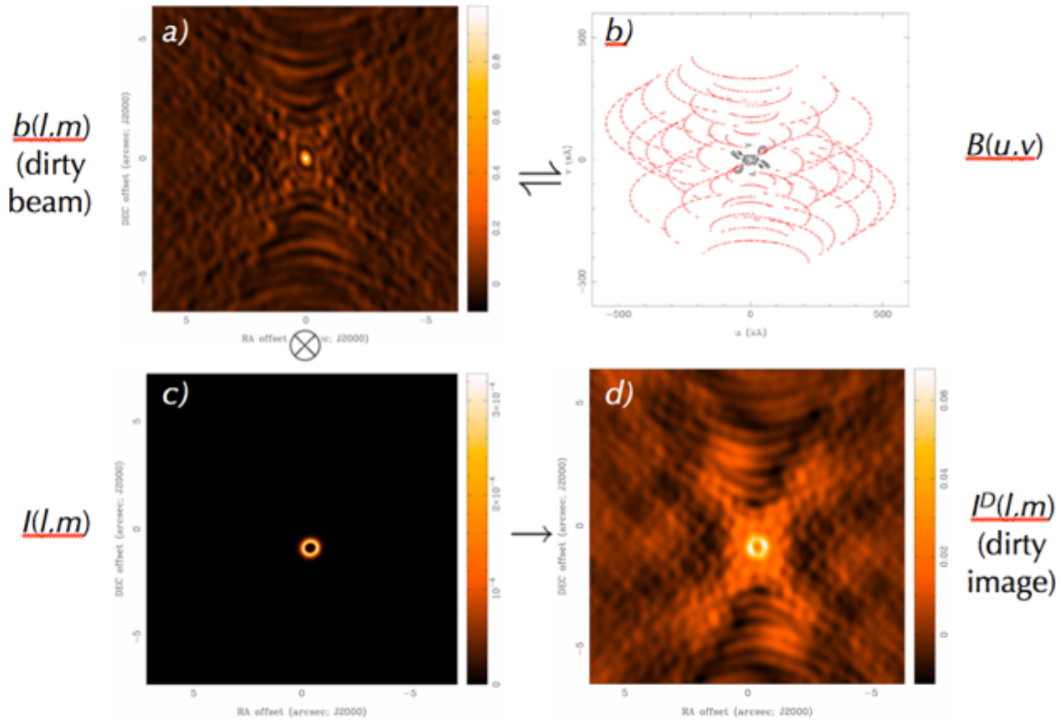

Figure 4.5: Imaging concepts. (a) Example dirty beam, $b(l, m)$; (b) discrete points sampled in the (u, v) plane, $B(u, v)$ (black: compact configuration, red: extended configuration); (c) example true sky distribution, $I(l, m)$; (d) dirty image $I^D(l, m)$ resulting from the convolution of $I(l, m)$ by $b(l, m)$. (Figure courtesy of D. Wilner.)

where ν is the observing frequency, and $\theta_{\rm max}$, $\theta_{\rm min}$ are the major and minor axes of the synthesized beam.

4.4 Data reduction and analysis

4.4.1 APEX

After being calibrated, the data can be further reduced and analysed using the CLASS, GREG and MAPPING packages included in the GILDAS software. For example, the continuum was removed by subtracting a baseline of a polynomial of order 1 for individual scans and spectral smoothing. Gaussian fitting to each line gives a peak intensity and line width. The integrated line intensity is calculated using the formula,

$$I_{\rm line} = \sum_{\rm i} I_{\rm i} dv, \tag{4.4}$$

where I is the intensity at each velocity and dv is the velocity resolution. The line-free frequency range in a spectrum gives its root mean square (rms) error for each sideband.

The error for the integrated line intensity is calculated using the formula,

$$\Delta I_{\rm line} = \sqrt{(\Delta I_{\rm L})^2 + (\Delta I_{\rm B})^2} = \sqrt{(\sigma v_{\rm res}\sqrt{N_{\rm L}})^2 + (\sigma v_{\rm res} N_{\rm L}/\sqrt{N_{\rm B}})^2}, \quad (4.5)$$

where σ is the rms noise level, $v_{\rm res}$ is the velocity resolution, $N_{\rm L}$ is the number of channels that contribute to the line, and $N_{\rm B}$ is the number of channels that are outside the emission line.

4.4.2 NOEMA

The calibration and imaging of the NOEMA data was performed within the CLIC and MAPPING packages of the GILDAS software[5], respectively. After the results of the pipeline calibration are reviewed and the visibilities are imported into MAPPING for non-pipeline imaging. Using the CLEAN task in MAPPING, the final data cubes are created. Further analysis (e.g., data resampling, moment maps, pv diagrams, etc.) is also performed using the same software package.

4.4.3 ALMA

The calibration of the ALMA data was done following standard procedures using the ALMA pipeline[6]. This is done by the observatory before the data delivery. In order to re-image and resample the data cubes to a different spectral resolution, the visibilities data were retrieved from the ALMA archive and then re-imaged using the Common Astronomy Software Applications (CASA) package[7], which is specifically developed and maintained for ALMA data processing. For the re-imaging process we used the task tclean of CASA. The final data cubes were then used for the scientific analysis of the data from which I derived physical parameters.

[5] http://www.iram.fr/IRAMFR/GILDAS

[6] `https://almascience.eso.org/processing/alma_pipeline_user_s_guide_for_release_2024-1.pdf`

[7] `https://casa.nrao.edu`

CHAPTER 5

Characterisation of Physical Parameters

5.1 Radiative Transfer modelling

General references: Radiative Processes in Astrophysics by Rybicki & Lightman (2004)

5.1.1 Radiative Transfer Fundamentals

The analysis of molecular line emission begins with defining key physical quantities. The *specific intensity* I_ν, measured in $\mathrm{W\,m^{-2}\,Hz^{-1}\,sr^{-1}}$, represents the energy received per unit frequency, area, time, and solid angle:

$$I_\nu = \frac{dE}{d\nu\, dA\, dt\, d\Omega}. \tag{5.1}$$

It characterises the directional distribution of radiation and is independent of the observer's distance from the source, thus encoding the intrinsic spatial structure of the emission.

Although the intensity is independent of the observer's distance, it can be modified when the radiation passes through intervening material. The change of the specific intensity I_ν along a path through a medium is governed by the radiative transfer equation:

$$\frac{dI_\nu}{ds} = -\alpha_\nu I_\nu + j_\nu, \tag{5.2}$$

where α_ν is the absorption coefficient and j_ν the emission coefficient. Introducing the

optical depth $\tau_\nu = \int \alpha_\nu \, ds$, the equation above can be written as

$$\frac{dI_\nu}{d\tau_\nu} = -I_\nu + \mathcal{S}_\nu, \tag{5.3}$$

with $\mathcal{S}_\nu = j_\nu/\alpha_\nu$ denoting the source function.

The formal solution for a slab with background intensity $I_{\nu,\mathrm{bg}}$ is

$$I_\nu = I_{\nu,\mathrm{bg}}\, e^{-\tau_\nu} + \int_0^{\tau_\nu} \mathcal{S}_\nu(\tau')\, e^{-(\tau_\nu - \tau')}\, d\tau', \tag{5.4}$$

which accounts for attenuation of background radiation and cumulative in-situ emission along the line of sight.

In radio astronomy it is convenient to express the specific intensity in terms of a *brightness temperature* T_b, defined implicitly by

$$I_\nu \;\equiv\; B_\nu(T_b),$$

where $B_\nu(T)$ is the Planck function,

$$B_\nu(T) \;=\; \frac{2h\nu^3}{c^2}\,\frac{1}{\exp\!\left(\frac{h\nu}{kT}\right) - 1}.$$

This definition states that T_b is the temperature that a blackbody must have for its Planck brightness to equal the measured I_ν at frequency ν.

When $h\nu \ll kT_b$, one has the Rayleigh-Jeans approximation where the Planck function reduces to $B_\nu(T) \simeq 2k\nu^2 T/c^2$, and it is common to introduce the concept of *radiation temperature* T_R via

$$I_\nu \;\equiv\; \frac{2k\nu^2}{c^2}\, T_\mathrm{R}.$$

In the Rayleigh-Jeans limit $h\nu \ll kT_b$, $T_\mathrm{R} \approx T_b$; outside this limit, $T_\mathrm{R} < T_b$ and the difference grows with frequency.

Another important concept is the *flux density* S_ν[1], measured in Jansky (Jy)[2]. The flux density is obtained by integrating the specific intensity over the source solid angle:

$$S_\nu = \int I_\nu \, d\Omega, \tag{5.5}$$

and, by definition, it quantifies the total energy received per unit frequency, area, and time:

$$S_\nu = \frac{dE}{d\nu\, dA\, dt}. \tag{5.6}$$

However, in radio astronomy it is common to quantify the observed signals as *antenna temperature* T_A, which is linked to the received power as $P_\mathrm{source} = k\, T_A\, \Delta\nu$. The antenna temperature is the beam-weighted average (convolution) of the source radiation temperature with the antenna power pattern:

[1] Not to be confused with the source function $\mathcal{S}_\nu$, despite the similar notation.
[2] $1\ \mathrm{Jy} \equiv 10^{-23}\,\mathrm{erg\,s^{-1}\,cm^{-2}\,Hz^{-1}}$.

$$T_A \;=\; \frac{\displaystyle\int_{4\pi} T_R(\hat{\boldsymbol{s}})\, P_n(\hat{\boldsymbol{s}})\, d\Omega}{\displaystyle\int_{4\pi} P_n(\hat{\boldsymbol{s}})\, d\Omega} \;=\; \frac{1}{\Omega_A}\int_{4\pi} T_R(\hat{\boldsymbol{s}})\, P_n(\hat{\boldsymbol{s}})\, d\Omega, \tag{5.7}$$

where P_n is the (peak-normalised) antenna power pattern and $\Omega_A \equiv \int_{4\pi} P_n\, d\Omega$ is the antenna beam solid angle.

Since one of the main characterising parameters of the radio telescope is its main beam, it is also convenient to define the *main beam temperature*

$$T_{\rm mb} \;\equiv\; \frac{\displaystyle\int_{4\pi} T_R(\hat{\boldsymbol{s}})\, P_n(\hat{\boldsymbol{s}})\, d\Omega}{\displaystyle\int_{\Omega_{\rm mb}} P_n(\hat{\boldsymbol{s}})\, d\Omega} = \frac{T_A}{\eta_{\rm mb}}, \tag{5.8}$$

with main-beam efficiency $\eta_{\rm mb} \equiv \dfrac{\int_{\Omega_{\rm mb}} P_n\, d\Omega}{\Omega_A} = \frac{\Omega_{\rm mb}}{\Omega_A}$.

Given that $I_\nu = (2k\nu^2/c^2)\, T_R$, Eq.5.5 yields $S_\nu = \int I_\nu d\Omega = (2k\nu^2/c^2)\int T_R\, d\Omega$. Thus, for a source whose solid angle, Ω_s, is smaller than the main beam, the flux density is given by

$$S_\nu = \frac{2k\nu^2}{c^2}\, T_{\rm R}\, \Omega_s = \frac{2k\nu^2}{c^2}\, T_{\rm mb}\, \Omega_{\rm mb}, \tag{5.9}$$

which leads to the following relation between the radiation temperature and the main beam and antenna temperatures

$$T_{\rm R} = T_{\rm mb}\, \frac{\Omega_{\rm mb}}{\Omega_s} = \frac{T_A}{\eta_{\rm mb}}\, \frac{\Omega_{\rm mb}}{\Omega_s}. \tag{5.10}$$

Finally, we can use the definition of radiation temperature to relate the antenna temperature, which is a measured quantity, with the intensity in the following way:

$$I_\nu \;= \frac{2k\nu^2}{c^2}\, \frac{T_A}{\eta_{\rm mb}}\, \frac{\Omega_{\rm mb}}{\Omega_s}. \tag{5.11}$$

5.1.2 Solving Radiative Transfer Problems

Statistical Equilibrium

A common approach to solving the integral in Equation 5.4 is to assume that the source function $\mathcal{S}_\nu$ is given by the Planck function evaluated at the excitation temperature $T_{\rm ex}$:

$$\mathcal{S}_\nu = B_\nu(T_{\rm ex}) = \frac{2h\nu^3}{c^2}\, \frac{1}{e^{h\nu/kT_{\rm ex}} - 1}. \tag{5.12}$$

This approximation is valid under conditions of local thermodynamic equilibrium (LTE), where the molecular level populations follow a Boltzmann distribution at a common tem-

perature $T_{\rm ex}$.

However, in many astrophysical environments, LTE does not hold, and the source function must be computed explicitly from the level populations, which requires solving the statistical equilibrium equations. For a two-level system, the balance between radiative and collisional transitions is described by:

$$n_1(B_{12}\bar{J} + C_{12}) = n_2(A_{21} + B_{21}\bar{J} + C_{21}), \tag{5.13}$$

where n_1 and n_2 are the populations of the lower and upper energy levels, B_{ij} and A_{21} are the Einstein coefficients for absorption, stimulated emission, and spontaneous emission, respectively, $\bar{J}$ is the line-profile-averaged mean intensity of the radiation field, and C_{ij} are the collisional excitation and de-excitation rates.

The collisional rates satisfy the principle of detailed balance:

$$\frac{C_{12}}{C_{21}} = \frac{g_2}{g_1} e^{-\Delta E/kT}, \tag{5.14}$$

where g_i are the statistical weights of the energy levels, ΔE is the energy difference between the levels, and T is the kinetic temperature of the colliding particles (typically H_2 in molecular gas).

Solving the statistical equilibrium equations for multi-level systems requires a radiative transfer code, as the level populations depend on both local conditions and the radiation field, which in turn depends on the populations—a problem that must be solved iteratively.

Optically Thin Approximation

When line optical depths are low ($\tau \ll 1$), radiation fields minimally affect level populations. This simplifies calculations, as $\bar{J} \approx B_\nu(T_{\rm bg})$. However, this approximation fails for saturated lines or high-density regions.

Local Thermal Equilibrium (LTE)

As mentioned above, under LTE, level populations follow the Boltzmann distribution:

$$\frac{n_2}{n_1} = \frac{g_2}{g_1} e^{-h\nu/kT_{\rm kin}}. \tag{5.15}$$

The critical density $n_{\rm crit} = A_{21}/K_{21}$ determines when collisions dominate over spontaneous decay. For $n \gg n_{\rm crit}$, thermalisation occurs, and $T_{\rm ex} \approx T_{\rm kin}$. While the LTE approximation is very convenient, most astronomical situations are not in LTE. Thus, for more accurate modelling we need to consider non-LTE condition.

5.1.3 Overview of the RADEX Programme

RADEX[3] is a widely used computational tool for analysing interstellar molecular line spectra under non-local thermodynamic equilibrium (non-LTE) conditions. Originally developed by John Black and later refined by Van Der Tak et al. (2007), RADEX provides

[3] `https://home.strw.leidenuniv.nl/~moldata/radex.html`

rapid estimates of physical parameters of the interstellar medium—such as gas density, kinetic temperature, and column density—by modelling the intensities of observed molecular transitions. The code employs the escape probability formalism, assuming a homogeneous, isothermal medium without large-scale velocity gradients. Designed for computational efficiency, RADEX is particularly well suited for interpreting large datasets from modern radio and submillimetre telescopes. While it can optionally assume LTE conditions (i.e., a Boltzmann distribution of level populations) for quick estimates at high densities, its default operation is tailored for non-LTE analysis, which is essential in low-density environments where radiative processes dominate over collisional ones.

Methodology

The programme solves statistical equilibrium equations for molecular energy level populations, considering:

- Collisional excitation/de-excitation (using rate coefficients from the Leiden Atomic & Molecular Database, LAMDA[4])
- Radiative transitions (spontaneous emission, absorption, stimulated emission)
- Background radiation fields (e.g., cosmic microwave background)

Optical depth effects are treated via the escape probability approximation(Langevelde & van der Tak 1994), which simplifies radiative transfer by assuming photons either escape immediately or are absorbed locally. For a homogeneous medium, the optical depth τ_ν relates to the escape probability β as:

$$\beta = \frac{1 - e^{-\tau_\nu}}{\tau_\nu}$$

RADEX iteratively computes level populations until convergence, using initial optically thin estimates to derive τ_ν and update excitation conditions.

Input Parameters & Output

To model molecular line emission using RADEX, five key parameters must be specified. The kinetic temperature ($T_{\rm kin}$) and molecular hydrogen density ($n_{\rm H_2}$) define the thermal and collisional environment governing energy transfer processes. The molecular column density ($N_{\rm mol}$), typically expressed in cm^{-2}, determines the optical depth of transitions and scales the overall emission strength. Observations are further characterised by the line width (Δv, full width at half maximum in km s^{-1}), which influences photon trapping efficiency through velocity broadening. Lastly, the background radiation temperature ($T_{\rm bg}$) accounts for external illumination sources, including the cosmic microwave background (2.73 K) and optional contributions from dust or nearby stars. These parameters collectively constrain the statistical equilibrium solutions for molecular energy level populations and resultant line fluxes.

The RADEX calculations yield several critical parameters for interpreting molecular line observations. The line radiation temperatures ($T_{\rm R}$), expressed in Kelvin, represent the

[4] `https://home.strw.leidenuniv.nl/~moldata/`

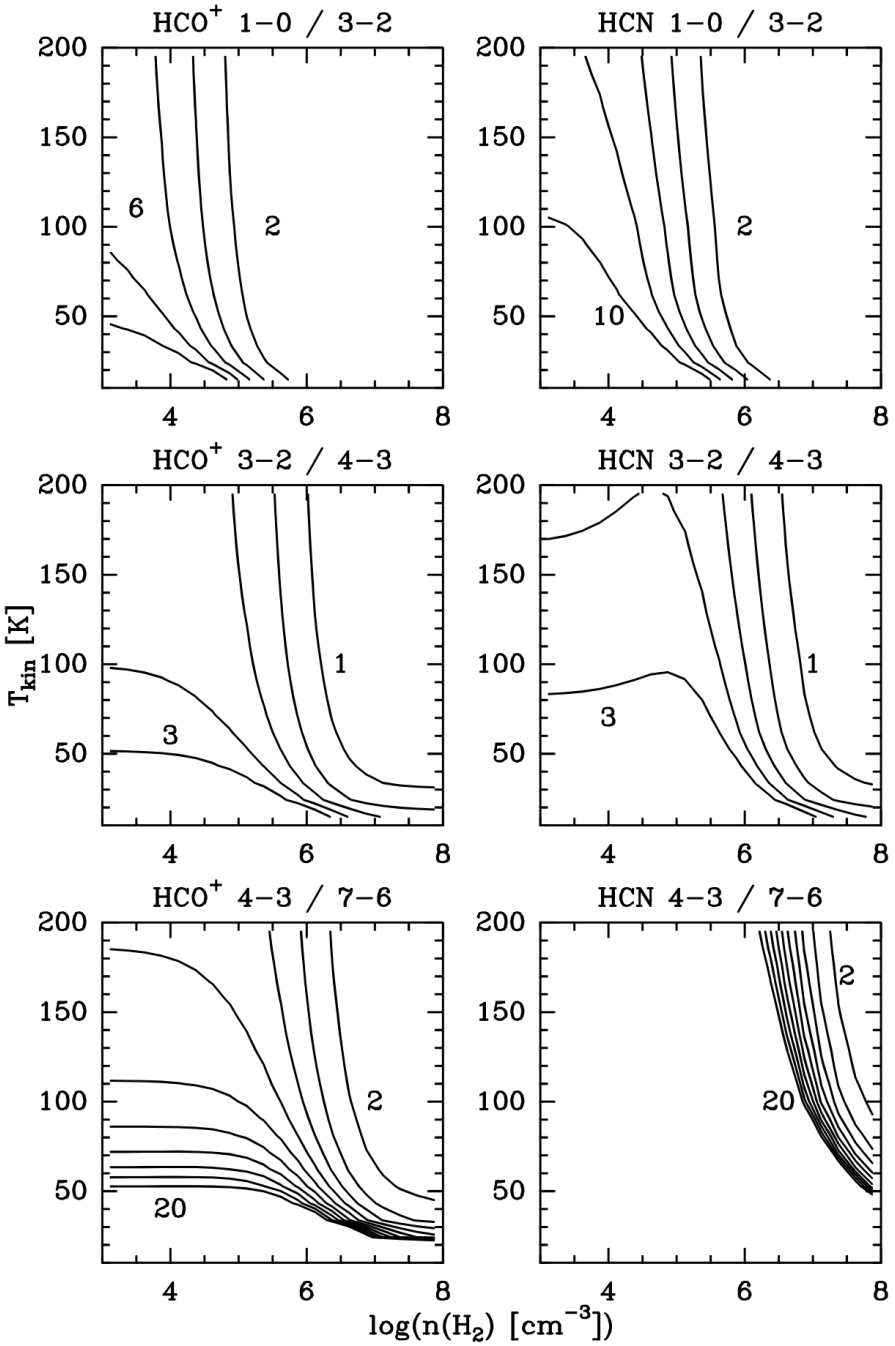

Figure 5.1: Example diagnostic plot for HCN line ratios, demonstrating how RADEX constrains density and temperature (Van Der Tak et al. 2007).

observed brightness temperatures of transitions, directly comparable to telescope measurements. Optical depths (τ) quantify the transparency of each transition, with $\tau \ll 1$ in-

dicating optically thin emission and $\tau > 1$ significant photon trapping. Excitation temperatures ($T_{\rm ex}$) characterise the thermal population distribution across energy levels, deviating from the kinetic temperature ($T_{\rm kin}$) under non-LTE conditions. Critical densities ($n_{\rm crit} = A_{ul}/C_{ul}$) demarcate the threshold where collisional de-excitation rates match spontaneous emission, below which radiative processes dominate. These outputs collectively enable determination of gas physical conditions (density, temperature) and molecular abundances through comparison with observational data. Fig.5.1 shows an example diagnostic plot for HCN line ratios, demonstrating how RADEX constrains density and temperature.

Applications & Limitations

RADEX finds extensive application in determining physical conditions within interstellar and circumstellar environments. The code enables derivation of gas densities spanning 10^2–$10^8\,{\rm cm}^{-3}$ and kinetic temperatures between 5–500 K through comparison of modelled and observed line intensities. A key application lies in estimating molecular abundances by matching column densities to emission line strengths, particularly when multiple transitions are available. The interpretation of line ratios, such as those between CO isotopologues (^{12}CO/^{13}CO) or density-sensitive species like HCN and HCO$^+$, provides critical diagnostics of excitation conditions and chemical evolution.

However, several limitations affect its applicability. The assumption of homogeneous density and temperature distributions becomes problematic in clumpy or structured media, where gradients significantly alter excitation conditions. Velocity gradients, which influence photon escape probabilities through Doppler shifts, are not accounted for in the current implementation. Perhaps most critically, the accuracy of RADEX solutions depends fundamentally on the quality of collisional rate coefficients sourced from databases like LAMDA – uncertainties in these rates propagate directly into derived physical parameters, particularly for complex organic molecules with sparse laboratory data.

5.2 Kinematic modelling

By studying the velocity field of gas, it is possible to identify distinct kinematic structures associated with different components of astronomical sources. Characterisation of the velocity field is achieved through analysis of molecular spectral emission. However, from our standpoint, we can only measure the line-of-sight component of the velocity vector. To reconstruct the three-dimensional distribution of the gas, spatial-kinematic modelling becomes necessary. To investigate the gas dynamics in the nuclear region of the galaxy NGC 4418, I used the computational modelling tool `FERIA` (Flat Envelope model with Rotation and Infall under Angular momentum conservation; Oya et al. 2022). `FERIA` is specifically designed for the spatial-kinematic analysis of disc-like gas distributions. It enables to reconstruct three-dimensional velocity fields from observed line-of-sight velocities by parametrically modelling rotational and infall motions under the assumption of angular momentum conservation.

5.2.1 Overview of the FERIA Programme

General reference: Oya et al. (2022)

`FERIA` was originally developed to model disc-like structures around protostars. However, its underlying principles are equally applicable to galactic-scale kinematics, particularly in the central regions of galaxies where analogous dynamical processes occur. The model's framework considers two key components observed in both protostellar and galactic systems: (i) infalling-rotating structure, and (ii) Keplarian-disk-like rotation (Fig.5.2).

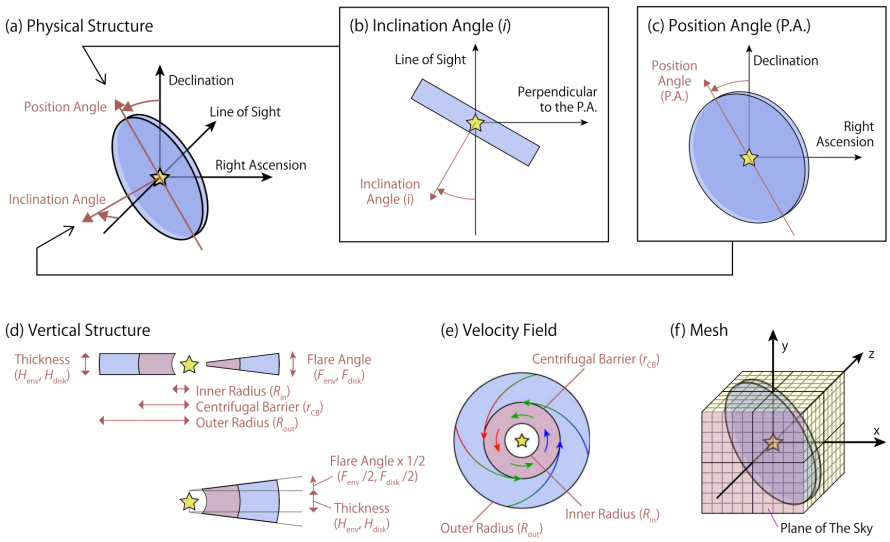

Figure 5.2: Schematic illustration of the infalling-rotating envelope and Keplerian disk models (Oya et al. 2022). More details in the Fig.1 of Oya et al. (2022).

Adaptations for Extragalactic Studies

The `FERIA` model, originally developed for analysing protostellar systems (100–1000 au scales), can be adapted for studying galactic nuclei by changing the interpretation for some of the parameters. Its dimensionless formulation allows for scalability to 1–100 pc scales by preserving key dynamical ratios, such as those between centrifugal radii and system sizes, through the rescaling of parameters.

Table 5.1 lists the input parameters for `FERIA` that are interpreted in the context for galactic nuclei.

Geometric & Kinematic Structure

The model assumes an axisymmetric system with an inclination angle i and position angle (P.A.). For radii greater than the centrifugal barrier ($r > r_{\rm CB}$), the envelope component follows infall-rotation governed by the conservation of angular momentum and energy. The

Protostar	Galactic Centre
Central protostar mass (M)	Supermassive black hole (SMBH) mass
Centrifugal barrier (r_{CB})	Transition radius between inflow and nuclear disk
Envelope density ($\rho \propto r^{-1.5}$)	Power-law gas distributions in galactic nuclei

Table 5.1: Comparison between protostellar and galactic context parameters.

centrifugal barrier radius is defined as:

$$r_{\mathrm{CB}} = \frac{j^2}{2GM},$$

where j is the specific angular momentum and M the central mass. The rotational and infall velocities at radius r are derived as:

$$v_{\mathrm{rot}} = \frac{j}{r} = \frac{1}{r}\sqrt{2GMr_{\mathrm{CB}}},$$

$$v_{\mathrm{fall}} = \sqrt{\frac{2GM}{r} - v_{\mathrm{rot}}^2}.$$

For radii interior to the centrifugal barrier ($r < r_{\mathrm{CB}}$), the disk component follows pure Keplerian rotation:

$$v_{\mathrm{Kep}} = \sqrt{\frac{GM}{r}}.$$

The transition at r_{CB} is characterised by the cessation of infall motion ($v_{\mathrm{fall}} = 0$), making the boundary between envelope dynamics and disk-dominated kinematics. This method neglects pressure gradients, magnetic fields, self-gravity, and turbulence, focusing purely on gravitational and angular momentum effects. Density (ρ) and temperature (T) distributions are prescribed as power-law functions of radius ($r^{\alpha_{\mathrm{dens}}}$ and $r^{\alpha_{\mathrm{temp}}}$ respectively), rather than being dynamically calculated. Radiative transfer effects are omitted, with emission assumed optically thin and line profiles approximated as Gaussians. Furthermore, instrumental resolution effects are simulated through homogeneous beam convolution, which simplifies the spatial filtering process but does not account for direction-dependent variations in real interferometric data.

Numerical Implementation

The numerical method in `FERIA` uses a structured procedure to make synthetic data for comparison with observations. The three-dimensional structure is divided into grids for space and velocity, where the positions are given by (x, y, z) and the velocities are grouped by channel size, corresponding to the spectral resolution. For each pixel, the code calculates the emission along the line of sight, using power-law profiles for density and temperature.

To simulate the effects of the telescope, the data is blurred in space and velocity using the Fast Fourier Transform, with a Gaussian beam for spatial resolution and a set line width for velocity resolution. The main results are common data products such as moment maps (integrated intensity and velocity) and position-velocity diagrams, all saved as FITS files that can be directly compared to actual observations.

Limitations: Artefacts can appear if the grid is too coarse near r_{CB} or if the spatial and spectral resolution is not high enough.

CHAPTER 6

Outlook and future works

6.1 Summary of paper I

In this paper, we report observations of the H_2S 1_{10}–1_{01} emission line (ν = 168.763 GHz) towards 12 nearby galaxies. The observations were executed using the APEX single dish telescope. Our aim was to find out how luminous the H_2S ground state emission is in dusty, luminous galaxies and if this can be related to the prevalence and properties of outflows. To further investigate the origin and distribution of H_2S emission, we also observed the H_2S 1_{10}–1_{01} emission line at higher spatial resolution towards the ULIRG Mrk 231 using the NOEMA interferometer.

We detected the H_2S 1_{10}–1_{01} emission line in 10 out of 13 galaxies (including in Mrk 231 with NOEMA). This supports the notion that ground state H_2S line emission is relatively common in (U)LIRGs. We compared the H_2S/HCN line intensity ratio among the galaxies in our sample and did not find any increase of the H_2S abundance (in relation to HCN) associated with the existence of outflows in the galaxies. On the other hand, when we compare H_2S, HCN, HCO^+ (as dense gas tracers) and CO (as a global molecular mass tracer), the line luminosity of the H_2S has a stronger correlation with the molecular mass of outflows than CO in the sample galaxies. We discuss that this indicates the direct relation of the H_2S molecule in outflows and the host galaxy reservoir. We also compared the $L_{H_2S} - L_{IR}$ correlation to that previously found between higher excitation H_2O and IR (Yang et al. 2013), and found them to be similar.

My contribution to Paper I included the design and writing of the proposal for the APEX observations. Furthermore, I carried out all the reduction and analysis of the spectral data,

except for the data reduction of the NOEMA data which was performed by S. König. I wrote the manuscript, with the exception of the text in section 2.3, which was provided by S. König.

6.2 Summary of paper II

In this paper, we report ALMA observations of the ortho-H_2S 1_{10}–1_{01} emission line towards the nearby galaxies NGC 1377, NGC 4418, and NGC 1266. These observations achieve a spatial resolution of ∼0".5, a much smaller scale than the previous APEX single-dish data (∼37"), enabling precise localisation of H_2S emission on sub-arcsecond scales. By combining these data with archival H_2S $2_{2,0}$–$2_{1,1}$ (216.710 GHz) observations, we aim to constrain the physical conditions of gas-phase H_2S excitation by radiative transfer modelling.

We detect compact H_2S emission in all three galaxies, originating from regions smaller than ∼300 pc. The spectral profiles exhibit broad line wings ($\Delta v \gtrsim 100$ km s^{-1}), indicative of outflowing or shocked gas. In NGC 4418, the H_2S kinematics reveal counterrotating gas components, alongside a peculiar redshifted emission feature that may trace inflowing material or a slanted outflow.

RADEX modelling of the H_2S transitions yields gas densities $n_{H_2} \gtrsim 10^7$ cm^{-3} and temperatures $T_{kin} = 40$–200 K. These densities exceed those inferred from CO observations by 1 to 2 orders of magnitude, suggesting that H_2S selectively traces the densest regions of the interstellar medium. The elevated temperatures and kinematic complexity suggest energy injection from shocks or radiative heating, probably associated with AGN or compact starburst activity. This work establishes H_2S as a sensitive probe of extreme physical conditions in galaxy nuclei, with implications for understanding feedback-driven gas dynamics in dusty environments.

My contribution to Paper II included preparing the proposal of the ALMA observations for NGC 1377 and NGC 1266. I carried out the full analysis of the data including imaging, continuum subtraction, spectral and continuum analysis, and the radiative transfer modelling from RADEX. I performed all the ALMA data reduction except for the data of NGC 4418, which was performed by S. König. I wrote the manuscript.

6.3 Summary of paper III

In this paper, we describe an observational study of the luminous infrared galaxy NGC4418 using ALMA with a spatial resolution of ∼0".05, focusing on the emission of the H_2S. It enables to resolve the nuclear region down to scales of about 8 parsec. The goal is to understand how H_2S relates to dense gas structures and shock activity near the galaxy's nucleus.

The H_2S emission is detected within a 0".2 region of the galactic nucleus, showing a clumpy, ring-like structure with weaker emission at the nucleus itself, indicating possible absorption or strongly varying physical conditions. High-velocity, red- and blue-shifted H_2S components are found on opposite sides of the nucleus and do not align with the main disk rotation, suggesting complex kinematics. To characterise the kinematic parameters, we employed a program `FERIA`, which considers an inflowing-rotating envelope. The data

cube and the position-velocity (PV) diagrams from the observations agree with the models assuming an inflowing-rotating disk with some features that the models cannot fully explain, such as strong counter-rotating emission appearing in the observed PV diagram along the major axis. This may point to enhanced H_2S in inflowing gas, possibly influenced by shocks.

The H_2S-to-HNC emission ratio helps identify regions where shocks are likely important. Methanol, another molecule released during intense shocks, appears in regions slightly displaced from H_2S and HNC peaks, supporting the scenario where shock chemistry changes molecular abundances on small scales. Water emission is also present but not correlated with the main H_2S features.

My contribution to Paper III included performing the full scientific analysis of the H_2S data cube from ALMA, spectral and continuum analysis, and the kinematic modelling with `FERIA`. The reduction of the ALMA data including other molecular lines was performed by S. König. I wrote the manuscript with the exception of section 4, for which S. Aalto provided the initial text.

6.4 Future work

While the work presented in this thesis provide new insights on the origin and behaviour of H_2S in obscured nuclei of nearby galaxies, several questions remain open and require further investigation.

First, radiative transfer modelling including additional transitions of H_2S and other species would allow us to better constrain excitation conditions. This would deepen our understanding of the environments in which H_2S is enhanced and provide a more quantitative link between observed emission and physical processes behind it.

Kinematic modelling also has substantial room for improvement. In particular, combining radiative transfer with a model that accounts for not only a single infalling-rotating structure but also multiple kinematic components might be necessary to reproduce the observed distribution and velocity field of H_2S, for example for dusty galactic centres such as NGC 4418. Improving these models will be key to better picturise the kinematics traced by H_2S.

A broader and equally important step forward is to extend the analysis to a larger sample of galaxies. Applying the same techniques used in this thesis to a wider range of environments, including different levels of obscuration, star formation rates, and AGN activity, will help determine whether the enhancement of H_2S is a general tracer of nuclear feedback or specific to a particular class of infrared-luminous systems. Such a sample would also enable statistical correlations between H_2S, dense gas tracers, and outflow signatures.

Additional observational tracers can further clarify the chemical and excitation conditions that lead to H_2S. Combining H_2S with other sulphur-bearing molecules (e.g., SO, SO_2, CS) as well as shock tracers (e.g., SiO) could offer better constrains to the physical conditions in the regions of interest. Future high-resolution observations with the new capabilities of ALMA and other interferometers will be crucial in detecting these species across a range of physical scales.

Finally, chemical modelling remains an open major challenge. As described in Chap. 2.4, the formation mechanisms of H_2S involve multiple competing pathways whose efficiencies depend on grain mantle chemistry, temperature, shock strength, and radiation. A dedicated

chemical modelling effort will be necessary to disentangle these processes and to robustly interpret the abundance enhancements observed in this work.

Altogether, these future directions have the potential to place the results of this thesis into a broader astrophysical context, clarifying both the role of H_2S as a probe of nuclear feedback and the life cycle of dense gas in infrared-luminous galaxies.

References

Aalto, S. et al. (2011). "H3O+ line emission from starbursts and AGNs". *Astronomy and Astrophysics* 527.8, pp. 1–8. ISSN: 00046361.

Aalto, S et al. (2012). "Winds of change – a molecular outflow in NGC 1377 ? The anatomy of an extreme FIR-excess galaxy". 68, pp. 1–10.

Aalto, S. et al. (2015a). " High resolution observations of HCN and HCO + J = 3–2 in the disk and outflow of Mrk 231 ". *Astronomy & Astrophysics* 574, A85. ISSN: 0004-6361.

Aalto, S. et al. (2015b). "Probing highly obscured, self-absorbed galaxy nuclei with vibrationally excited HCN". *Astronomy and Astrophysics* 584. ISSN: 14320746.

Aalto, S. et al. (2016). "A precessing molecular jet signaling an obscured, growing supermassive black hole in NGC 1377?" *Astronomy and Astrophysics* 590. ISSN: 14320746.

Aalto, S. et al. (Dec. 2017). "Luminous, pc-scale CO 6-5 emission in the obscured nucleus of NGC 1377". *Astronomy and Astrophysics* 608. ISSN: 14320746.

Aalto, S. et al. (2019). "The hidden heart of the luminous infrared galaxy IC 860: I. A molecular inflow feeding opaque, extreme nuclear activity". *Astronomy and Astrophysics* 627. ISSN: 14320746.

Aalto, S. et al. (Aug. 2020). "ALMA resolves the remarkable molecular jet and rotating wind in the extremely radio-quiet galaxy NGC 1377". *Astronomy and Astrophysics* 640. ISSN: 14320746.

Aalto, S. (2012). "Molecules as tracers of galaxy evolution". *Proceedings of the International Astronomical Union* 8.S292, pp. 199–208. ISSN: 17439213.

Aladro, R. et al. (Sept. 2018). "Molecular gas in the northern nucleus of Mrk 273: Physical and chemical properties of the disc and its outflow". *Astronomy and Astrophysics* 617. ISSN: 14320746.

Alatalo, K. et al. (2011). "Discovery of an active galactic nucleus driven molecular outflow in the local early-type galaxy NGC 1266". *Astrophysical Journal* 735.2. ISSN: 15384357.

Alatalo, K. (Mar. 2015). "Escape, accretion, or star formation? the competing depleters of gas in the quasar markarian 231". *Astrophysical Journal Letters* 801.1. ISSN: 20418213.

Arroyave, A., Cicone, C., et al. (2024). "A possible relation between global CO excitation and massive molecular outflows in local ULIRGs". *Astronomy & Astrophysics* 685, A81.

Bachiller, R. et al. (2001). "Chemically active outflow L 1157". *Astronomy and Astrophysics* 372.3, pp. 899–912. ISSN: 00046361.

Banzatti, A. (2013). "Water vapor distribution in protoplanetary disks". *Doctral Thesis in ETH Zurich*. ISSN: 15384357.

Barcos-Muñoz, L. et al. (2018). "Fast, Collimated Outflow in the Western Nucleus of Arp 220". *The Astrophysical Journal* 853.2, p. L28. ISSN: 2041-8213.

Belitsky, V et al. (2018). "SEPIA - A new single pixel receiver at the APEX telescope Citation for the original published paper (version of record): Astrophysics SEPIA – a new single pixel receiver at the APEX telescope".

Charnley, S. B. (1997). "Sulfuretted Molecules in Hot Cores". *The Astrophysical Journal* 481.1, pp. 396–405. ISSN: 0004-637X.

Cicone, C. et al. (2012). "The physics and the structure of the quasar-driven outflow in Mrk 231". *Astronomy and Astrophysics* 543. ISSN: 00046361.

Cicone, C. et al. (2014). "Massive molecular outflows and evidence for AGN feedback from CO observations". *Astronomy and Astrophysics* 562, pp. 1–25. ISSN: 00046361.

Cicone, C. et al. (Aug. 2018). " ALMA [C i] 3 P 1 – 3 P 0 Observations of NGC 6240: A Puzzling Molecular Outflow, and the Role of Outflows in the Global α CO Factor of (U)LIRGs ". *The Astrophysical Journal* 863.2, p. 143. ISSN: 0004-637X.

Cicone, C. et al. (2020). "Enhanced UV radiation and dense clumps in the molecular outflow of Mrk 231". *Astronomy & Astrophysics* 633, A163. ISSN: 0004-6361.

Combes, F. et al. (2014). "Erratum: ALMA observations of feeding and feedback in nearby Seyfert galaxies: An AGN-driven outflow in NGC? 1433 (Corrigendum)". *Astronomy and Astrophysics* 564, pp. 1–11. ISSN: 14320746.

Cornwell, T. J. (June 2009). *Hogbom's CLEAN algorithm. Impact on astronomy and beyond.*

Costagliola, F. et al. (2013). "High-resolution mm and cm study of the obscured LIRG NGC 4418: A compact obscured nucleus fed by in-falling gas?" *Astronomy and Astrophysics* 556. ISSN: 00046361.

Crockett, N. R. et al. (2014). "Herschel observations of extra-ordinary sources: H 2 S as a probe of dense gas and possibly hidden luminosity toward the orion kl hot core". *Astrophysical Journal* 781.2. ISSN: 15384357.

Dasyra, K. M. et al. (2016). "ALMA reveals optically thin, highly excited CO gas in the jet-driven winds of the galaxy IC 5063". *Astronomy and Astrophysics* 595, pp. 2–5. ISSN: 14320746.

Esplugues, G. B. et al. (2014). "Modelling the sulphur chemistry evolution in Orion KL". *Astronomy and Astrophysics* 567, pp. 1–14. ISSN: 14320746.

Falstad, N. et al. (2018). "Hidden molecular outflow in the LIRG Zw 049.057". *Astronomy and Astrophysics* 609. ISSN: 14320746.

Falstad, N. et al. (2019). "Hidden or missing outflows in highly obscured galaxy nuclei?" *Astronomy and Astrophysics* 623. ISSN: 14320746.

Falstad, N. et al. (2021). "CON-quest Searching for the most obscured galaxy nuclei". 105, pp. 1–16.

Faucher-Giguère, C. A. & Quataert, E. (Sept. 2012). "The physics of galactic winds driven by active galactic nuclei". *Monthly Notices of the Royal Astronomical Society* 425.1, pp. 605–622. ISSN: 13652966.

Ferrara, A. & Scannapieco, E. (2016). "on the Formation of Molecular Clumps in Qso Outflows". *The Astrophysical Journal* 833.1, p. 46. ISSN: 1538-4357.

Feruglio, C. et al. (2010). "Quasar feedback revealed by giant molecular outflows". *Astronomy and Astrophysics* 518.13, pp. 1–4. ISSN: 00046361.

Feruglio, C et al. (2013). "NGC 6240 : extended CO structures and their association". 51.

Fluetsch, A. et al. (Aug. 2021). "Properties of the multiphase outflows in local (ultra)luminous infrared galaxies". *Monthly Notices of the Royal Astronomical Society* 505.4, pp. 5753–5783. ISSN: 13652966.

Gao, Y. & Solomon, P. M. (2004a). "HCN Survey of Normal Spiral, Infrared-luminous, and Ultraluminous Galaxies". *The Astrophysical Journal Supplement Series* 152.1, pp. 63–80. ISSN: 0067-0049.

– (2004b). "The Star Formation Rate and Dense Molecular Gas in Galaxies". *The Astrophysical Journal* 606.1, pp. 271–290. ISSN: 0004-637X.

Gao, Y. et al. (June 2021). "The Nuclear Region of NGC 1365: Star Formation, Negative Feedback, and Outflow Structure". *The Astrophysical Journal* 913.2, p. 139. ISSN: 0004-637X.

García-Burillo, S. et al. (2014). "Molecular line emission in NGC 1068 imaged with ALMA : I. An AGN-driven outflow in the dense molecular gas". *Astronomy and Astrophysics* 567, pp. 1–24. ISSN: 14320746.

García-Burillo, S. et al. (Aug. 2015). "High-resolution imaging of the molecular outflows in two mergers: IRAS 17208-0014 and NGC 1614". *Astronomy and Astrophysics* 580. ISSN: 14320746.

Goicoechea, J. R. et al. (Mar. 2021). "Bottlenecks to interstellar sulfur chemistry: Sulfur-bearing hydrides in UV-illuminated gas and grains". *Astronomy and Astrophysics* 647. ISSN: 14320746.

Goldsmith, P. F. & Kauffmann, J. (May 2017). "Electron Excitation of High Dipole Moment Molecules Re-examined". *The Astrophysical Journal* 841.1, p. 25. ISSN: 0004-637X.

González-Alfonso, E. et al. (2012). "Herschel /PACS spectroscopy of NGC 4418 and Arp 220: H 2O, H 218O, OH, 18OH, O? I, HCN, and NH 3". *Astronomy and Astrophysics* 541. ISSN: 00046361.

Harada, N. et al. (2018). "ALMA Astrochemical Observations of the Infrared-luminous Merger NGC 3256". *The Astrophysical Journal* 855.1, p. 49.

Hatchell, J. & Viti, S. (2002). "Possible evidence for shocks in hot cores". *Astronomy and Astrophysics* 381.1. ISSN: 00046361.

Heikkilä, A., Johansson, L. E., & Olofsson, H. (1999). "Molecular abundance variations in the Magellanic Clouds". *Astronomy and Astrophysics* 344.3, pp. 817–847. ISSN: 00046361.

Henkel, C. et al. (2018). "Molecular line emission in NGC 4945, imaged with ALMA". *Astronomy and Astrophysics* 615. ISSN: 14320746.

Herpin, F. et al. (2009). "S-bearing molecules in massive dense cores". *Astronomy and Astrophysics* 504.3, pp. 853–867. ISSN: 14320746.

Hil, M. J. & Zakamska, N. L. (2014). "Warm molecular hydrogen in outflows from ultraluminous infrared galaxies". *Monthly Notices of the Royal Astronomical Society* 439.3, pp. 2701–2716. ISSN: 13652966.

Holdship, J et al. (2017). "UCLCHEM : A Gas-grain Chemical Code for Clouds , Cores , and C-Shocks *". *The Astronomical Journal* 154.1, p. 38. ISSN: 1538-3881.

Imanishi, M. & Nakanishi, K. (Oct. 2013). "Alma detection of the vibrationally excited HCN J = 4-3 emission line in the Agn-hosting luminous Infrared Galaxy Iras 20551-4250". *Astronomical Journal* 146.4. ISSN: 00046256.

Imanishi, M., Nakanishi, K., & Izumi, T. (July 2016). " ALMA INVESTIGATION OF VIBRATIONALLY EXCITED HCN/HCO + /HNC EMISSION LINES IN THE AGN-HOSTING ULTRALUMINOUS INFRARED GALAXY IRAS 205514250 ". *The Astrophysical Journal* 825.1, p. 44. ISSN: 0004-637X.

Impellizzeri, C. M. V. et al. (Oct. 2019). "Counter-rotation and High-velocity Outflow in the Parsec-scale Molecular Torus of NGC 1068". *The Astrophysical Journal Letters* 884.2, p. L28. ISSN: 2041-8205.

Israel, F. P. et al. (2023). "A multitransition survey of dense gas tracers HCN, HNC and HCO^+ in nearby galaxies". *Astronomy & Astrophysics* 672, A133.

Langevelde, H. Jan van & van der Tak, F. (1994). *Radiation Bookkeeping: a guide to astronomical molecular spectroscopy and radiative transfer problems with an emphasis on RADEX*. Tech. rep.

Leroy, A. K. et al. (Sept. 2015). "FAINT CO LINE WINGS in FOUR STAR-FORMING (ULTRA)LUMINOUS INFRARED GALAXIES". *Astrophysical Journal* 811.1. ISSN: 15384357.

Lindberg, J. E. et al. (2016). "Evidence for a chemically differentiated outflow in Mrk 231". *Astronomy and Astrophysics* 587, pp. 1–11. ISSN: 14320746.

Lo, K. Y. (2005). "MEGA-MASERS AND GALAXIES". *Annual Review of Astronomy and Astrophysics* 43.1, pp. 625–676.

Lutz, D. et al. (2020). "Molecular outflows in local galaxies: Method comparison and a role of intermittent AGN driving". *Astronomy & Astrophysics* 633, A134. ISSN: 0004-6361.

Maiolino, R. et al. (2017). "Star formation inside a galactic outflow". *Nature* 544.7649, pp. 202–206. ISSN: 14764687.

Martin, S. et al. (2005). "Sulfur Chemistry and Isotopic Ratios in the Starburst Galaxy NGC 253". *The Astrophysical Journal* 620.1, pp. 210–216. ISSN: 0004-637X.

Martín, S et al. (2011). "The Submillimeter Array 1 . 3 mm line survey of Arp 220". 36.

Martín, S et al. (2016). "Astrophysics The unbearable opaqueness of Arp220". *Astronomy & Astrophysics* 25, pp. 1–14.

Matsushita, S. et al. (Sept. 2015). "MOLECULAR GAS AND RADIO JET INTERACTION: A CASE STUDY OF THE SEYFERT 2 AGN M51". *Publications of The Korean Astronomical Society* 30.2, pp. 439–442. ISSN: 1225-1534.

Michiyama, T. et al. (2018). " ALMA Observations of HCN and HCO + Outflows in the Merging Galaxy NGC 3256 ". *The Astrophysical Journal* 868.2, p. 95.

Minh, Y. C. et al. (Sept. 1990). "Observations of the H2S toward OMC-1". *The Astrophysical Journal* 360.2, p. 136. ISSN: 0004-637X.

Minh, Y. C. et al. (June 2007). "Unveiling the Ongoing Star Formation in the Starburst Galaxy NGC 253". *The Astrophysical Journal* 661.2, pp. L135–L138. ISSN: 0004-637X.

Mitchell, G. F. (Dec. 1984). "Effects of shocks on the sulfur chemistry of a dense interstellar cloud". *The Astrophysical Journal* 287, p. 665. ISSN: 0004-637X.

Morganti, R. et al. (2015). "The fast molecular outflow in the Seyfert galaxy IC 5063 as seen by ALMA". *Astronomy and Astrophysics* 580. ISSN: 14320746.

Morganti, R. et al. (Sept. 2016). "Another piece of the puzzle: The fast H i outflow in Mrk 231". *Astronomy and Astrophysics* 593. ISSN: 14320746.

Murray, N., Quataert, E., & Thompson, T. A. (2005). "On the Maximum Luminosity of Galaxies and Their Central Black Holes: Feedback from Momentum-driven Winds". *The Astrophysical Journal* 618.2, pp. 569–585. ISSN: 0004-637X.

Nakai, N. et al. (1987). "A Nuclear Molecular Ring and Gas Outflow in the Galaxy M82". *Publications of the Astronomical Society of Japan* 39, pp. 685–708.

Navarro-Almaida, D. et al. (Apr. 2020b). "Gas phase Elemental abundances in Molecular cloudS (GEMS). II. On the quest for the sulphur reservoir in molecular clouds: the $H_{2}S$ case".

Navarro-Almaida, D. et al. (2020a). "Gas phase Elemental abundances in Molecular cloudS (GEMS) II. on the quest for the sulphur reservoir in molecular clouds: The H2S case". *Astronomy & Astrophysics* 39.637, A39. ISSN: 23318422.

Neufeld, D. A. & Dalgarno, A (1989). *FAST MOLECULAR SHOCKS. I. REFORMATION OF MOLECULES BEHIND A DISSOCIATIVE SHOCK*. Tech. rep., pp. 869–893.

Oba, Y. et al. (2019). "Physico-chemical Behavior of Hydrogen Sulfide Induced by Reactions with H and D Atoms on Different Types of Ice Surfaces at Low Temperature". *The Astrophysical Journal* 874.2, p. 124. ISSN: 1538-4357.

Oosterloo, T. et al. (Dec. 2017). "Properties of the molecular gas in the fast outflow in the Seyfert galaxy IC 5063". *Astronomy and Astrophysics* 608. ISSN: 14320746.

Oya, Y. et al. (Sept. 2022). "FERIA: Flat Envelope Model with Rotation and Infall under Angular Momentum Conservation". *Publications of the Astronomical Society of the Pacific* 134.1039. ISSN: 00046280.

Papadopoulos, P. P. (2007). " HCN versus HCO + as Dense Molecular Gas Mass Tracers in Luminous Infrared Galaxies ". *The Astrophysical Journal* 656.2, pp. 792–797. ISSN: 0004-637X.

Pardo, J. R., Cernicharo, J., & Serabyn, E. (Jan. 2001). "Atmospheric Transmission at Microwaves (ATM): An Improved Model for Millimeter/Submillimeter Applications". *IEEE Transactions on Antennas and Propagation* 49.12, p. 1683.

Pereira-Santaella, M. et al. (Oct. 2016). "High-velocity extended molecular outflow in the star-formation dominated luminous infrared galaxy ESO 320-G030". *Astronomy and Astrophysics* 594. ISSN: 14320746.

Pereira-Santaella, M. et al. (2018). "Spatially resolved cold molecular outflows in ULIRGs". *Astronomy and Astrophysics* 616, pp. 1–20. ISSN: 14320746.

Pérez-Torres, M. et al. (Dec. 2021). *Star formation and nuclear activity in luminous infrared galaxies: an infrared through radio review.*

Pineau-desForets, G. et al. (June 1993). "Sulphur-bearing molecules as tracers of shocks in interstellar clouds". *Monthly Notices of the Royal Astronomical Society* 262.4, pp. 915–928. ISSN: 0035-8711.

Privon, G. C. et al. (Feb. 2017). "The Dense Molecular Gas and Nuclear Activity in the ULIRG IRAS 13120–5453". *The Astrophysical Journal* 835.2, p. 213. ISSN: 0004-637X.

Rau, U. & Cornwell, T. J. (2011). "A multi-scale multi-frequency deconvolution algorithm for synthesis imaging in radio interferometry". *Astronomy and Astrophysics* 532. ISSN: 00046361.

Richings, A. J. & Faucher-Giguère, C. A. (Mar. 2018). "The origin of fast molecular outflows in quasars: Molecule formation in AGN-driven galactic winds". *Monthly Notices of the Royal Astronomical Society* 474.3, pp. 3673–3699. ISSN: 13652966.

Rybicki, G. B. & Lightman, A. P. (2004). *Radiative processes in astrophysics*. Wiley-VCH, p. 382. ISBN: 0471827592.

Saito, T. et al. (Mar. 2018). "Imaging the molecular outflows of the prototypical ULIRG NGC 6240 with ALMA". *Monthly Notices of the Royal Astronomical Society: Letters* 475.1, pp. L52–L56. ISSN: 17453933.

Sakamoto, K. et al. (Dec. 2010). "Vibrationally excited HCN in the luminous infrared galaxy NGC 4418". *Astrophysical Journal Letters* 725.2 PART 2. ISSN: 20418213.

Sakamoto, K. et al. (2013). "Submillimeter interferometry of the luminous infrared galaxy NGC 4418: A hidden hot nucleus with an inflow and an outflow". *Astrophysical Journal* 764.1. ISSN: 15384357.

Sakamoto, K. et al. (2014). "An infrared-luminous merger with two bipolar molecular outflows: ALMA and SMA observations of NGC 3256". *Astrophysical Journal* 797.90. ISSN: 15384357.

Salak, D. et al. (May 2016). "GAS DYNAMICS AND OUTFLOW IN THE BARRED STARBURST GALAXY NGC 1808 REVEALED WITH ALMA". *The Astrophysical Journal* 823.1, p. 68. ISSN: 0004-637X.

Sanders, D. B. & Mirabel, I. F. (1996). "LUMINOUS INFRARED GALAXIES", pp. 749–792.

Sato, M. T. et al. (Apr. 2022). "APEX and NOEMA observations of H2S in nearby luminous galaxies and the ULIRG Mrk 231: A possible relation between dense gas properties and molecular outflows". *Astronomy and Astrophysics* 660. ISSN: 14320746.

Scoville, N. et al. (Feb. 2017). "ALMA Resolves the Nuclear Disks of Arp 220". *The Astrophysical Journal* 836.1, p. 66. ISSN: 0004-637X.

Solomon, P. M. & Vanden Bout, P. A. (Sept. 2005). "Molecular Gas at High Redshift". *Annual Review of Astronomy and Astrophysics* 43.1, pp. 677–725.

Tafalla, M. et al. (Nov. 2010). "A molecular survey of outflow gas: Velocity-dependent shock chemistry and the peculiar composition of the EHV gas". *Astronomy and Astrophysics* 522.7. ISSN: 14320746.

Thaddeus, P. et al. (1972). "Interstellar Hydrogen Sulfide". *The Astrophysical Journal* 176.c, p. L73. ISSN: 0004-637X.

Tsai, A.-L. et al. (2009). *Molecular Superbubbles and Outflows from the Starburst Galaxy NGC 2146*. Tech. rep., pp. 237–250.

Tsai, A. L. et al. (June 2012). "First detection of a subkiloparsec scale molecular outflow in the starburst galaxy NGC3628". *Astrophysical Journal* 752.1. ISSN: 15384357.

Ulich, B. L. & Haasf, R. W. (1976). *ABSOLUTE CALIBRATION OF MILLIMETER-WAVELENGTH SPECTRAL LINES*. Tech. rep., pp. 247–258.

Van Der Tak, F. F. et al. (June 2007). "A computer program for fast non-LTE analysis of interstellar line spectra* with diagnostic plots to interpret observed line intensity ratios". *Astronomy and Astrophysics* 468.2, pp. 627–635. ISSN: 00046361.

Veilleux, S. et al. (2013). "Fast molecular outflows in luminous galaxy mergers: Evidence for quasar feedback from herschel". *Astrophysical Journal* 776.1. ISSN: 15384357.

Veilleux, S., Cecil, G., & Bland-Hawthorn, J. (2005). "Galactic Winds". *Annual Review of Astronomy and Astrophysics* 43.1, pp. 769–826.

Veilleux, S. et al. (Dec. 2020). *Cool outflows in galaxies and their implications.*

Venturi, G. et al. (Nov. 2017). "Ionized Gas Outflows from the MAGNUM Survey: NGC 1365 and NGC 4945". *Frontiers in Astronomy and Space Sciences* 4. ISSN: 2296987X.

Venturi, G. et al. (Nov. 2018). "MAGNUM survey: A MUSE- Chandra resolved view on ionized outflows and photoionization in the Seyfert galaxy NGC1365". *Astronomy and Astrophysics* 619. ISSN: 14320746.

Vidal, T. H. G. et al. (2017). "On the reservoir of sulphur in dark clouds: chemistry and elemental abundance reconciled". *Monthly Notices of the Royal Astronomical Society* 469.1, pp. 435–447. ISSN: 0035-8711.

Viti, S. et al. (2004). "Evaporation of ices near massive stars: Models based on laboratory temperature programmed desorption data". *Monthly Notices of the Royal Astronomical Society* 354.4, pp. 1141–1145. ISSN: 00358711.

Wakelam, V. et al. (2004). "Sulphur-bearing species in the star forming region L1689N". *Astronomy and Astrophysics* 413.2, pp. 609–622. ISSN: 00046361.

Walter, F. et al. (2017). "Dense Molecular Gas Tracers in the Outflow of the Starburst Galaxy NGC 253". *The Astrophysical Journal* 835.2, p. 265. ISSN: 1538-4357.

Woods, P. M. et al. (2015). "A new study of an old sink of sulphur in hot molecular cores: The sulphur residue". *Monthly Notices of the Royal Astronomical Society* 450.2, pp. 1256–1267. ISSN: 13652966.

Yang, C. et al. (July 2013). "Water vapor in nearby infrared galaxies as probed by herschel". *Astrophysical Journal Letters* 771.2. ISSN: 20418205.

Zschaechner, L. K. et al. (Dec. 2016). "THE MOLECULAR WIND IN THE NEAREST SEYFERT GALAXY CIRCINUS REVEALED BY ALMA". *The Astrophysical Journal* 832.2, p. 142. ISSN: 0004-637X.